GEOHORIZON

Organic matter–hosted pore system, Marcellus Formation (Devonian), Pennsylvania

Kitty L. Milliken, Mark Rudnicki, David N. Awwiller, and Tongwei Zhang

ABSTRACT

The Marcellus Formation of Pennsylvania represents an outstanding example of an organic matter (OM)–hosted pore system; most pores detectable by field-emission scanning electron microscopy (FE-SEM) are associated with OM instead of mineral matrix. In the two wells studied here, total organic carbon (TOC) content is a stronger control on OM-hosted porosity than is thermal maturity. The two study wells span a maturity from late wet gas (vitrinite reflectance [R_o], ~1.0%) to dry gas (R_o, ~2.1%). Samples with a TOC less than 5.5 wt. % display a positive correlation between TOC and porosity, but samples with a TOC greater than 5.5 wt. % display little or no increase in porosity with a further increasing TOC. In a subset of samples (14) across a range of TOC (2.3–13.6 wt. %), the pore volume detectable by FE-SEM is a small fraction of total porosity, ranging from 2 to 32% of the helium porosity. Importantly, the FE-SEM–visible porosity in OM decreases significantly with increasing TOC, diminishing from 30% of OM volume to less than 1% of OM volume across the range of TOC. The morphology and size of OM-hosted pores also vary systematically with TOC.

The interpretation of this anticorrelation between OM content and SEM-visible pores remains uncertain. Samples with the lowest OM porosity (higher TOC) may represent gas expulsion (pore collapse) that was more complete as a consequence of greater OM connectivity and framework compaction,

Manuscript received March 9, 2012; provisional acceptance June 13, 2012; revised manuscript received June 28, 2012; final acceptance July 23, 2012.
DOI:10.1306/07231212048

AUTHORS

KITTY L. MILLIKEN ~ *Bureau of Economic Geology, Jackson School of Geosciences, University of Texas at Austin, Austin, Texas; kittym@mail.utexas.edu*

Kitty Milliken is a senior research scientist at the Bureau of Economic Geology at the University of Texas at Austin. She holds a B.A. degree in geology from Vanderbilt University and an M.A. degree and a Ph.D. in geology from the University of Texas at Austin. Her research has centered on the diagenesis of sedimentary rocks. She is a member of the graduate studies committee of the Jackson School of Geosciences and supervises graduate students in the area of mudrock petrology.

MARK RUDNICKI ~ *ExxonMobil Upstream Research Company, Houston, Texas; mark.d.rudnicki@exxonmobil.com*

Mark Rudnicki is a research scientist in the unconventional gas and tight oil reservoir characterizaton integrated project at ExxonMobil Upstream Research Company. He holds a B.Sc. degree in geology from the University of Sheffield, United Kingdom and a Ph.D. in marine geochemistry from the University of Cambridge, United Kingdom His research involves understanding the reservoir quality properties of mudstones that are capable of producing gas and liquids.

DAVID N. AWWILLER ~ *ExxonMobil Upstream Research Company, Houston, Texas; david.n.awwiller@exxonmobil.com*

David N. Awwiller is a senior research associate at ExxonMobil Upstream Research Company. His expertise is in reservoir quality characterization and prediction, low-temperature geochemistry, and diagenesis. He holds a B.A. degree in geology from Case Western Reserve University and a Ph.D. in geology from the University of Texas at Austin.

TONGWEI ZHANG ~ *Bureau of Economic Geology, Jackson School of Geosciences, University of Texas at Austin, Austin, Texas; tongwei.zhang@beg.utexas.edu*

Tongwei Zhang is a research associate and organic geochemist at the Bureau of Economic Geology, University of Texas at Austin. He holds a B.S. degree in geology and a Ph.D. in isotope

geochemistry and completed postdoctoral work in chemistry at Caltech. His research focuses on the geology of petroleum and natural gas, shale gas geochemistry, and CO2 sequestration.

ACKNOWLEDGEMENTS

This study is a product of the ExxonMobil–Bureau of Economic Geology Collaborative Project for Unconventional Resources (2008–2011). We thank Rob Reed and Xiaohu Tang for assistance with argon-milling and scanning electron microscopy imaging. We also thank Svetlana Ikonnikova for providing helpful advice on analysis of statistical distributions. We thank Barbara Faulkner for supporting our project with many behind-the-scenes efforts to garner institutional support. The publication was approved by the director of the Bureau of Economic Geology.

The AAPG Editor thanks the following reviewers for their work on this paper: Martin J. Evans, Bruce Hart, and Michael L. Sweet.

whereas samples with higher OM porosity (lower TOC) correspond to rigid mineral frameworks that inhibited compactional expulsion of methane-filled bubbles. Alternatively, higher TOC samples may contain OM (low initial hydrogen index, relatively unreactive) that is less prone to development of FE-SEM–detectable pores. In this interpretation, OM type, controlled by sequence-stratigraphic position, is a factor in determining pore-size distribution.

INTRODUCTION

Pores within organic matter (OM) are widely recognized as a significant component of pore systems in gas shales (Loucks et al., 2009; Ambrose et al., 2010; Passey et al., 2010; Sondergeld et al., 2010b; Curtis et al., 2011a, b; Slatt and O'Brien, 2011; Milliken et al., 2012a). Although other pore types are also important in gas shales, and in mudrocks generally (Schieber, 2010; Slatt and O'Brien, 2011; Loucks et al., 2012), the contribution of OM-hosted pores to overall porosity is such that the total organic carbon (TOC) manifests a positive covariation with bulk porosity in some gas shale units (Passey et al., 2010; Milliken et al., 2012a).

The discovery of OM-hosted pore systems sparks many questions concerning their nature and prediction: To what degree are these pore systems primary (hosted within initially porous kerogen) versus secondary (formed during diagenesis)? If secondary, can the evolution of OM-hosted pores be linked quantitatively to the well-established thermal maturation trends that are documented for OM? What is the function of OM type in the occurrence and diagenetic evolution of OM-hosted pore systems? The answers to these questions are central to making predictions of rock properties in mudrock-hosted petroleum systems.

This study applies integrated scanning electron microscope (SEM) imaging and bulk analysis to assess the qualitative and quantitative aspects of both mineral- and OM-hosted pores in siliciclastic-dominated mudrocks of the Marcellus Formation of northern Pennsylvania. Samples come from two wells of contrasting thermal maturity (R_o of ~1.0% versus 2.1%) and contain a prominent component of OM-hosted pores. Our results point to some unexpected conclusions concerning the function of thermal maturation in the evolution of OM-hosted porosity and highlight some deficiencies in our understanding of organic petrography at the scale of SEM observations.

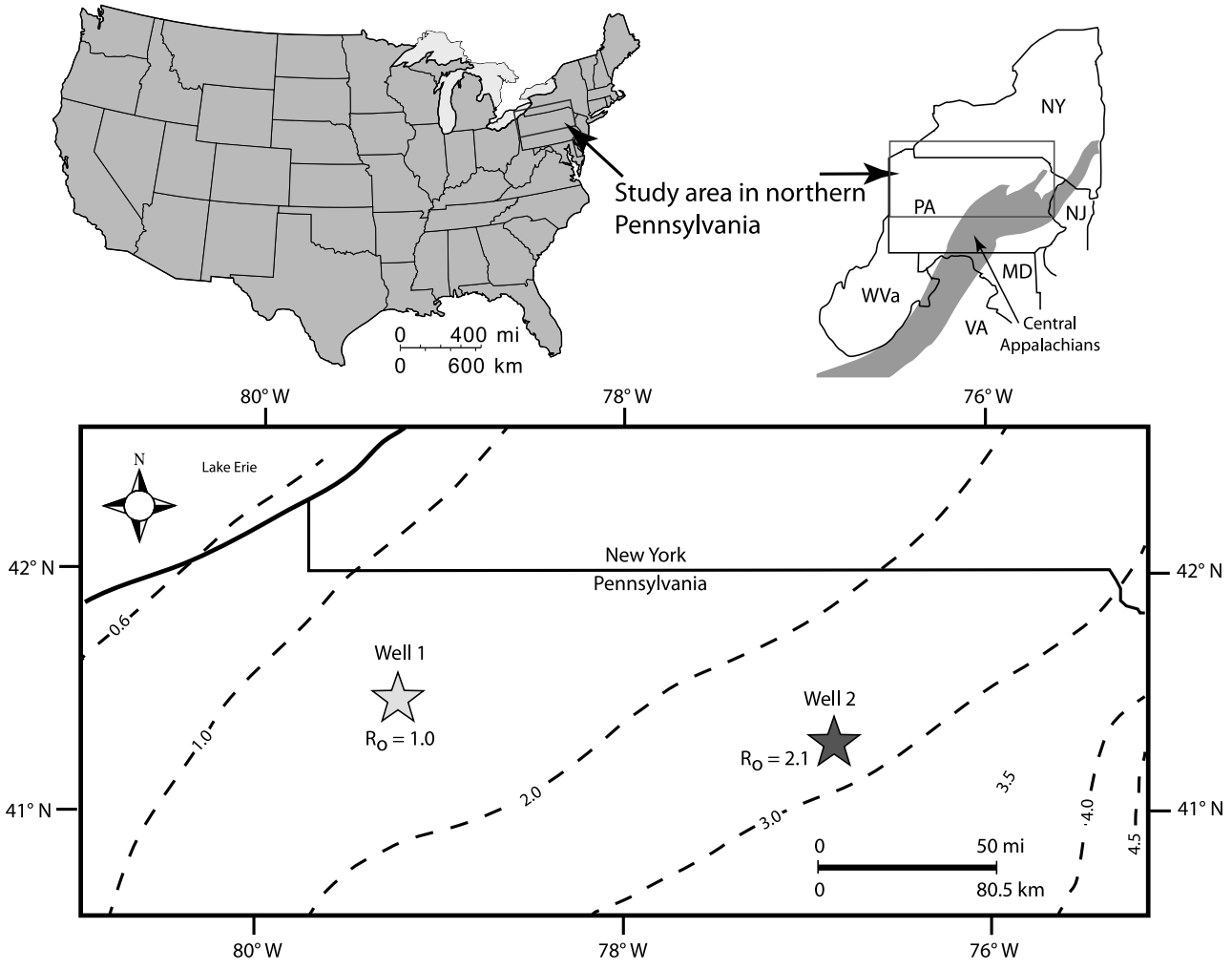

Figure 1. Locations of the two study wells. Contours depict thermal maturity (contoured on regional averages of vitrinite reflectance [R_o]). The inset map on the upper left side (modified from Gray and Stamatakos, 1997) depicts the position of the study area relative to the Alleghanian front of the central Appalachians. NY = New York; PA = Pennsylvania; NJ = New Jersey; MD = Maryland; VA = Virginia; WVa = West Virginia.

GEOLOGIC SETTING

The Middle Devonian Marcellus Formation, the basal unit of the Hamilton Group, is a distal marine mudstone within a westward-prograding foreland succession deposited in the Appalachian Basin during the Acadian orogeny (Ettensohn, 1985; Lash and Engelder, 2011). Maximum burial was achieved in the late Paleozoic and was greatest along the thrust front on the eastern side of the basin (Johnsson, 1986; Beaumont et al., 1987; Roden and Miller, 1989; Evans, 1995; Reed et al., 2005). In the region of well 1 (Figure 1), maximum burial was on the order of 3.5 km (2.2 mi) and maximum temperature was on the order of 120°C, whereas in the region of well 2, farther to the east, maximum burial and temperature were on the order of 6 km (4 mi) and 150°C, respectively (Beaumont et al., 1987; Roden and Miller, 1989). The Marcellus has recently attracted great attention as an important gas-producing unit (Engelder and Lash, 2009; Zagorski et al., 2010). Samples used in this study come from the lowermost part of the Marcellus, and in particular, the deepest and most TOC-rich samples in well 1 come from an interval of high gamma-ray response as shown in Engelder and Lash (2009, their figure 8, p. 68).

SAMPLING AND METHODS

Fourteen samples (chips from whole core) were selected from two wells in northern Pennsylvania (Figure 1)—nine samples from the lower maturity well (well 1) and five samples from the higher maturity well (well 2). Samples were selected to represent variation in TOC and to include the higher end of the range of TOC observed in these wells.

Uncovered polished thin sections for light microscopy and SEM imaging were produced (by Spectrum Petrographics) using surface impregnation with a low-viscosity impregnation medium before the final polish to reduce mechanical damage. Samples were examined in both transmitted and reflected polarized light on a conventional petrographic microscope. Carbon-coated thin sections were inspected using an FEI Nova NanoSEM 430 field-emission SEM (FE-SEM); all samples were examined using both secondary electron and backscattered electron (BSE) imaging. Additional observations were made using cathodoluminescence (Gatan ChromaCL detector) and x-ray mapping (twin 30 mm^2 Bruker XFlash silicon drift detector energy dispersive spectroscopy detectors), as needed for component identification and characterization.

Surfaces for imaging were also prepared by argon-ion cross section polishing (Leica EM TIC020 mill) using an accelerating voltage of 8 kV, a sample current of 2.8 mA, and a milling time of 10 hr. A conductive coating of iridium was applied to assist in control of charging during high-resolution imaging on the FEI Nova NanoSEM 430, an FE-SEM. At the highest magnification used in this study (image field width = 2 µm; machine magnification = 150,000×), topographic artifacts related to the iridium coating are visible, appearing as a generally cracked and scaly surface. For reasons that are poorly understood, but are most likely related to the contrasting electrostatic properties of different materials under ion bombardment, this coating artifact is more strongly developed on mineral surfaces than on OM. Together with the relatively smaller BSE signal from OM (note that, on flat polished surfaces, a substantial part of the total signal contrast relates to BSE emission even in images made with a secondary electron detector), the contrast in coating artifact

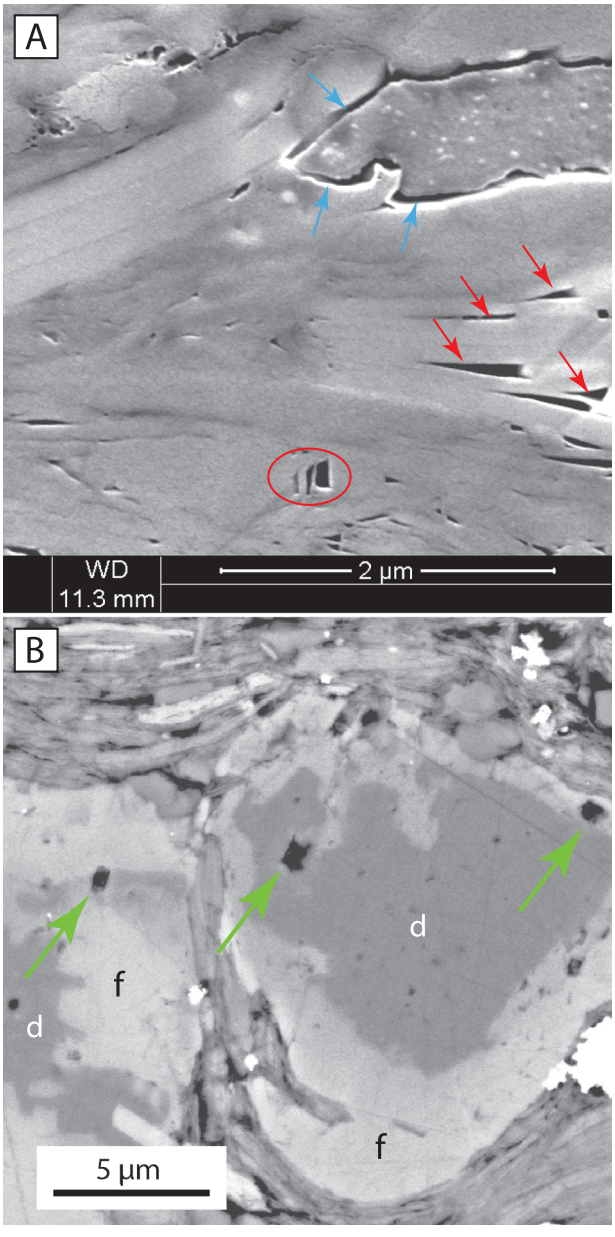

Figure 2. Mineral-surrounded pores. (A) Red arrows indicate pores that have opened between mica cleavage flakes. The red oval surrounds spaces between phyllosilicate flakes that are uncompacted beneath a silt particle. Blue arrows indicate a circumcrystalline pore on the margin of a carbonate particle. See text for discussion. Backscattered electron image. WD = working distance. (B) Green arrows indicate pores within crystals of dolomite (d) and ferroan dolomite (f). Whether these crystals represent grains, thereby hosting intragranular pores, or whether they are instead authigenic replacements containing intracrystalline pores is a matter for debate. Similar dolomite crystals in the Barnett Shale of central Texas have been interpreted as grains formed by erosion and reworking of early diagenetic dolomite (Milliken et al., 2012b). Backscattered electron image.

development assists in the discrimination of OM and mineral matter on argon-milled surfaces. Imaging of argon-milled surfaces was performed on an FEI NovaNano SEM 430 using an accelerating voltage of 10 kV and a spot size (sample current) of 3 (the instrument does not provide a quantitative readout of sample current; a setting of 3 is in the lower range of possible sample currents).

The general distribution of pores was examined in images captured at 19.9-μm horizontal field width (machine magnification = 15,000×; pixel resolution = 19.4 nm/pixel). Point counts (250 points) were made to determine the abundance of mineral crystals, OM, and mineral-hosted pores (Figure 2), but pores within OM are generally too small to be discerned at this magnification. Assessment of OM-hosted pores was made from images collected at 1.99-μm horizontal field width (machine magnification = 150,000×). These higher magnification images were obtained at either 1.9-nm or 0.97-nm pixel resolution, allowing for the reliable detection and interpretation of pores as small as 7 and 4 nm, respectively. Ten such images were obtained from randomly selected OM points in the lower magnification (15,000×) images. Edges of pores within OM were interpreted manually using a digital tracing screen (Wacom Cintiq pen display) and quantified using the image measurement program JMicrovision© (Roduit, 2008). JMicrovision includes routines for rendering interpreted shapes as objects for which a wide range of size and shape parameters are calculated (e.g., area, length, width, equivalent circular diameter, and others). A total of 28,004 pores were measured in the 140 images with 150,000× magnification. Pores were categorized based on size and shape following a scheme described below. Manual pore interpretation was used in preference to automated pore recognition to apply this categorization scheme and because image gray levels within pores significantly overlap gray levels displayed within sample defects (scratches and induced fractures) and within topographic artifacts in the conductive coating.

Observed porosity (SEM-imaged porosity), Φ_{obs}, is calculated:

$$\Phi_{obs} = (\text{Avg. } \Phi_{om} \times \text{OM vol. \%}) + \Phi_{min}$$

where Φ_{om} is the fraction of pore space measured within the overall volume of OM (averaged from the ten randomly selected regions of OM, imaged at 150,000×); OM vol. % is the volume percent of OM calculated from the measured bulk TOC (wt. %) by assuming an OM density of 1.45 g/cm^3; and Φ_{min} is the mineral-hosted porosity (vol. %) obtained from the point count at 15,000×.

Organic-matter–hosted pores are categorized into four groups based on size, shape, complexity, and spatial distribution (Figure 3). Most of the largest pores (reaching a little more than 1 μm in apparent diameter) are classed as complex. Complex pores have clearly discernible subparts, separated by partitions. Interpreting the boundaries of such pores necessarily entails encompassing a complex region into a single area that corresponds to the intersection of the pore with the plane of the milled surface. Complex pores tend to occur in clusters with other complex pores. A distinct subtype of pore occurs in direct or very close contact with a mineral surface and is designated a mineral-associated pore. Discrete spongelike pores lack the discernible subparts that characterize complex (and most mineral-associated pores) but still tend to occur in clusters and to display irregular nonequant shapes. Discrete spongelike pores range in size from the midrange of the complex pores (several tens of nanometers) to small sizes near the limit of detection (approximately 7 nm). Discrete isolated pores tend to be equant, widely distributed, and very small, ranging in size from the midrange of the discrete spongy pores (20–30 nm) to the limit of detection. Discrimination of the forgoing pore types is inherently somewhat subjective but, as demonstrated in the results section, allows discrimination of pore populations with distinctly different size distributions. These pore categorizations are put forth as a practical means of describing pore types solely for the purposes of this study and are not proposed as an extension or alternative to recently published generic pore classifications (Slatt and O'Brien, 2011; Loucks et al., 2012).

Cumulative distributions of the pore size, expressed in equivalent circular diameter, are compiled on the basis of both pore number and pore area (a proxy for volume in this two-dimensional

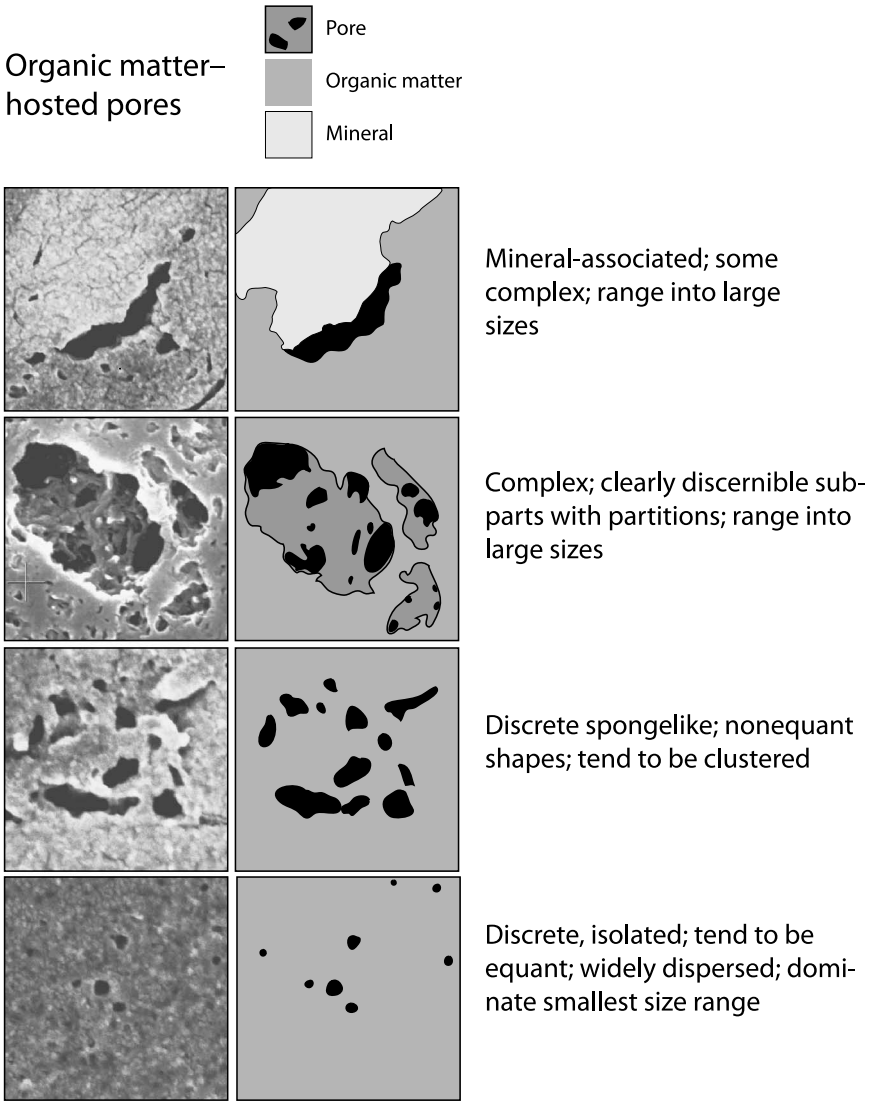

Figure 3. Qualitative categorization of OM-hosted pores, illustrated from secondary electron images (left) with interpreted line drawings (right). No scale is presented because the categories based on the forms illustrated apply across a range of scale. See text for discussion. Secondary electron images with a substantial backscattered electron component.

data set). Data presented as pore number are interesting for comparing the character of the pore populations in different samples, whereas the data compiled as pore area yield more direct insight into how the total pore volume is distributed across different size classes of pores.

BULK COMPOSITION AND BULK ROCK PROPERTIES

Data for bulk porosity, permeability, OM type, vitrinite reflectance, and whole-rock mineralogy by x-ray diffraction were obtained from TerraTek, Salt Lake City, Utah. Porosity and permeability data were generated by the tight rock analysis (TRA) procedure of TerraTek (Handwerger et al., 2011), which is modified from the crushed sample method of the Gas Research Institute (Luffel et al., 1996). Many issues and concerns surround the measurement of porosity and permeability in mudrocks, but the orderly trends observed in this study between bulk porosity measurements and independently measured parameters (see results section) indicate that the TRA data have, at least, relative significance.

RESULTS

Thermal Maturity

The average vitrinite reflectance values for two samples in well 1 are 0.96 (depth = 5011 ft [1527 m]) and 1.03 (depth = 5067 ft [1544 m]). Reflected light

observations noted an abundance of amorphinite as well as solid bitumen. The maturity for a sample in well 2 was determined by bituminite reflectance. Jacob's relationship, $R_V = 0.618\ R_B + 0.40$, where R_V = vitrinite reflectance and R_B = bituminite reflectance, (Jacob, 1989, p. 78) yields an equivalent R_o of approximately 2.1%. We regard this as a minimum value because it is now understood that different populations of pyrobitumen may have higher or lower reflectances compared to true vitrinite (Laughrey et al., 2011; slides 58–59).

Petrography

Mineral Components

Mudrocks examined in this study are silt-bearing mudstones (terminology of Macquaker and Adams, 2003) composed primarily of extrabasinal siliciclastic debris that includes illitic clay, mica, quartz, and feldspars (Figures 4, 5) (Table 1). Minor fossil components include conodonts, thin-walled bivalves, tentaculitids, stylolinids, tasmanitids, and agglutinated foraminifers. Calcite silt is abundant in samples 1 to 15 and is interpreted as comminuted skeletal debris. The most abundant and widespread authigenic components are pyrite framboids and euhedral pyrite replacing fossils (Figure 6A); bulk pyrite content averages 6.4 wt. % in well 1 and 4.2 wt. % in well 2 and ranges from 1.6 to 10.4 wt. %. Bulk pyrite displays a positive covariation with TOC. Ferroan dolomite euhedra are common, and many of these appear to be nucleated on detrital dolomite (Figure 6B). Quartz euhedra locally replace calcitic fossils (Figure 6C). In high-resolution SEM images, minute quartz crystals are observed lining OM-filled spaces (Figure 6D). Minor authigenic calcite is observed filling spores (see below).

Organic Matter

In light microscopy and in lower magnification SEM images, OM is observed in the form of particulate debris. A few samples contain spores that have been partially compacted (Figure 7A) or partially filled with calcite cement (Figure 7B). Many OM grains display sharply defined arcuate edges that are consistent with fragments formed by breakage of the porous structure of cellulosic (woody) material (Figure 7C). Organic material of clearly discrete particulate form but lacking definitive evidence as to a marine versus terrigenous origin is also observed (Figure 7D).

However, the greater proportion of OM in these rocks lacks the sharp edges and distinct shapes of particles. This dominant OM has homogenous texture, fills intergranular spaces uniformly (Figures 8A, 9B), and occurs within intergranular spaces partially lined by euhedral crystals (probable pore-filling cements) (Figure 7D). An effort to remove or partially mobilize this material with an organic solvent (dichloromethane) following argon-ion cross section polishing failed to yield any discernible change in the texture or porosity within this homogenous OM, although minor mobilization of OM from mineral-hosted pores may have occurred (Figure 9). Among the 140 images used for measurement of OM porosity, 138 feature this type of dispersed homogenous OM.

Pores

As discussed in the methods section, diverse pore types are observed, including both mineral-surrounded pores (Figure 2) and OM-hosted pores (Figure 3). Quantification of the subtypes of mineral-hosted pores was not attempted because these pores are minor overall (Table 1, data column Φ_{min}) and statistically significant measures would require point counting an exceedingly large number of points. A commonly observed form of mineral-surrounded pore occurs in association with micas and clays, representing spaces where phyllosilicate cleavage planes have been separated by the bending of a grain, as well as intergrain spaces held open where mica and/or clays have failed to compact into parallel arrangements (Figure 2A). Intracrystalline pores (Figure 2B) and, also, circumcrystalline pores (Figure 2A) are also common and are associated with carbonate particles, both calcite and dolomite. It is unknown if the intracrystalline pores are primary or secondary or if they are within grains or authigenic crystals, but the circumcrystalline pores are possibly related to postcoring dissolution caused by acid generation by sulfide oxidation. Evidence for this very abrupt mobilization of calcium from carbonate minerals is seen in the common calcium-sulfate precipitates that decorate even the argon-milled surfaces.

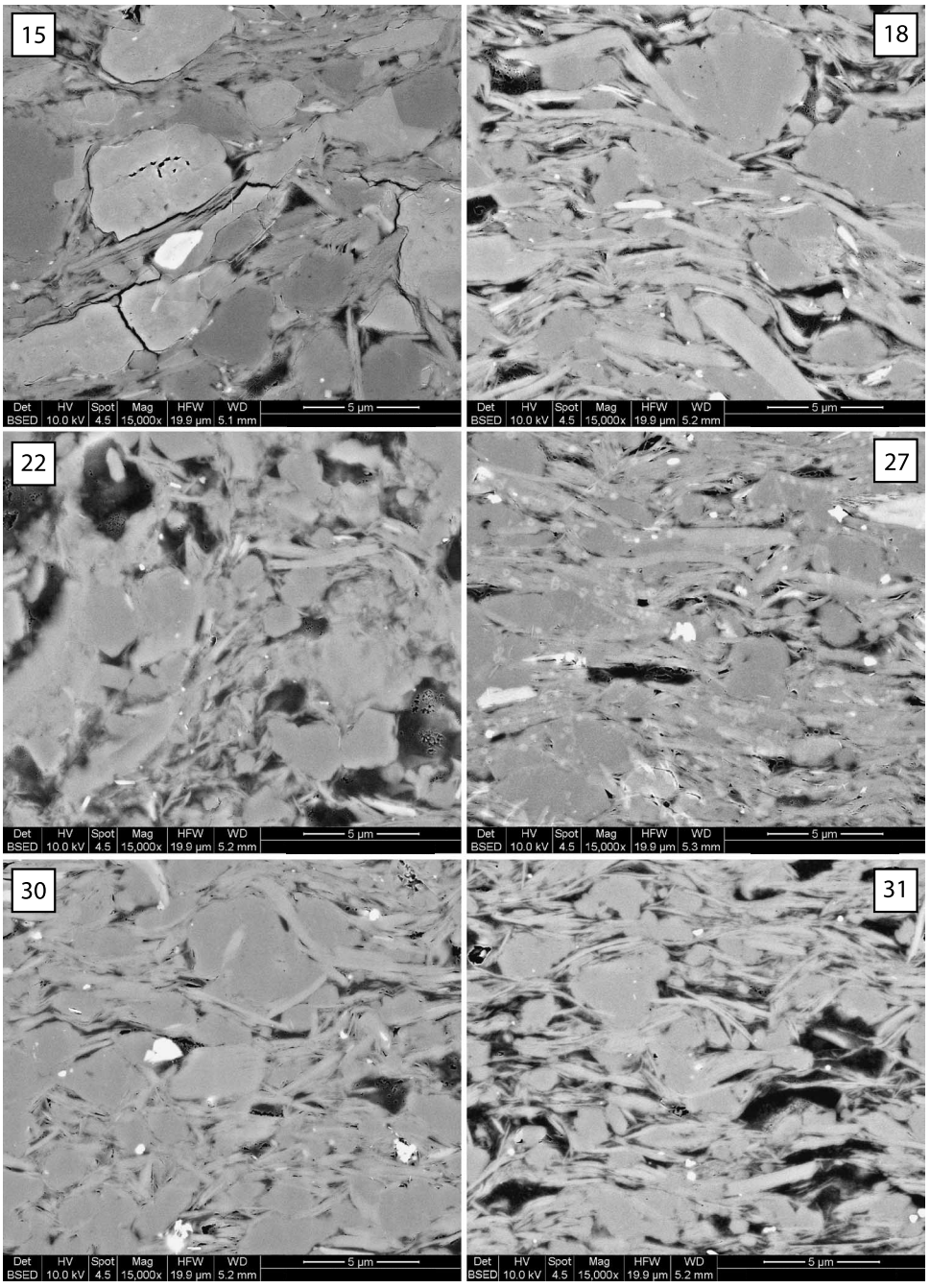

Figure 4. Backscattered electron images of samples from the lower maturity well. The numbers in the image corners correlate to the sample numbers in Tables 1 and 2. Overall, the samples are dominated by siliciclastic grains of quartz and feldspar (equant) and micas (elongate), with the exception of sample 15, which contains abundant calcite grains. The darkest regions of the images are mostly organic matter; the brightest regions (white) are pyrite. Det BSED = backscattered electron detector; HV = accelerating voltage; Spot = qualitative measure of beam current; WD = working distance; Mag = machine magnification; HFW = horizontal field width.

Among the OM-hosted pores, a common spatial clustering characterizes the complex, mineral-associated, and discrete spongelike pores. Many mineral-associated pores are also complex and tend to occur in groups and also in close spatial association with clusters of other larger pores. Linear groupings of larger pores with no immediately associated mineral surfaces are, in some cases, aligned with nearby mineral surfaces, suggesting that, in fact, these clusters are associated with mineral edges just below the plane of the section (Figure 10). Isolated equant pores, however, do not display the spatial associations of the three larger pore types and instead have a more uniform distribution.

Pores and Pore-Size Distributions

Overall, the Marcellus wells in this study present solid examples of pore systems that are strongly influenced by OM-hosted porosity (Figure 11). In both wells, a strong positive covariation of TOC

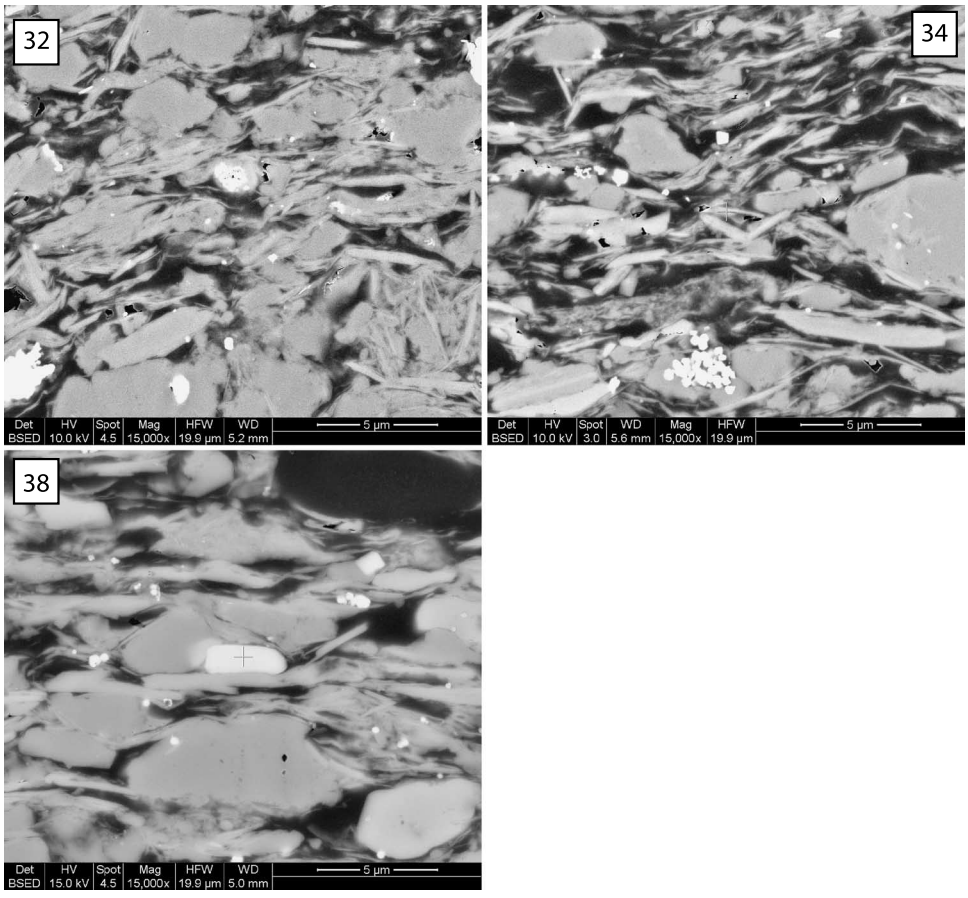

Figure 4. Continued

(as wt. %) and bulk porosity measured by helium porosimetry (as part of TRA) exists, the higher maturity well having somewhat less porosity for a given TOC content than does the lower maturity well (Figure 11). Trend lines for TOC versus porosity intersect a TOC of zero at a positive porosity, suggesting that the magnitude of non–OM-hosted porosity (i.e., mineral-hosted) in the overall sample set is approximately 3 vol. % in the low-maturity well and approximately 1 vol. % in the higher maturity well. The similar slopes of the TOC and bulk porosity trends at different maturities indicate that the OM-hosted porosity is grossly similar across the maturity range so that the greater porosity in the lower maturity well arises mostly from the greater content of mineral-hosted pores.

However, the positive covariation between TOC and bulk volume porosity does not extend to TOC content above approximately 5.5 wt. %. In the lower maturity well, at TOC contents above 5.5 wt. %, porosity drops from near 10 vol. % to approximately 7 vol. % and shows no further systematic variation across the remainder of the TOC range. In the higher maturity well, porosity continues to increase slightly through the higher TOC values, but above approximately 5.5 wt. %, the increase continues at a diminished rate with increasing TOC.

Data from high-resolution imaging help explain and further clarify the nature of the TOC and bulk porosity trends seen in Figure 11. Rocks of higher TOC have less detectable porosity within the OM (Figure 12A). Comparison with bulk porosity measurements indicates that pores above the detection limit for imaging (the sum of mineral-associated and OM-hosted pores) comprise only a fraction of the total pores and, thus, the proportion of total pores that are too small to image increases significantly with increasing TOC (Figure 12B). In the higher maturity well, for a given TOC, the OM-hosted porosity and the fraction of visible porosity is lower overall than in the lower maturity samples of equivalent TOC (Figure 12).

Cumulative pore-size distributions show that pore size (as mean, modal, and maximum sizes) also

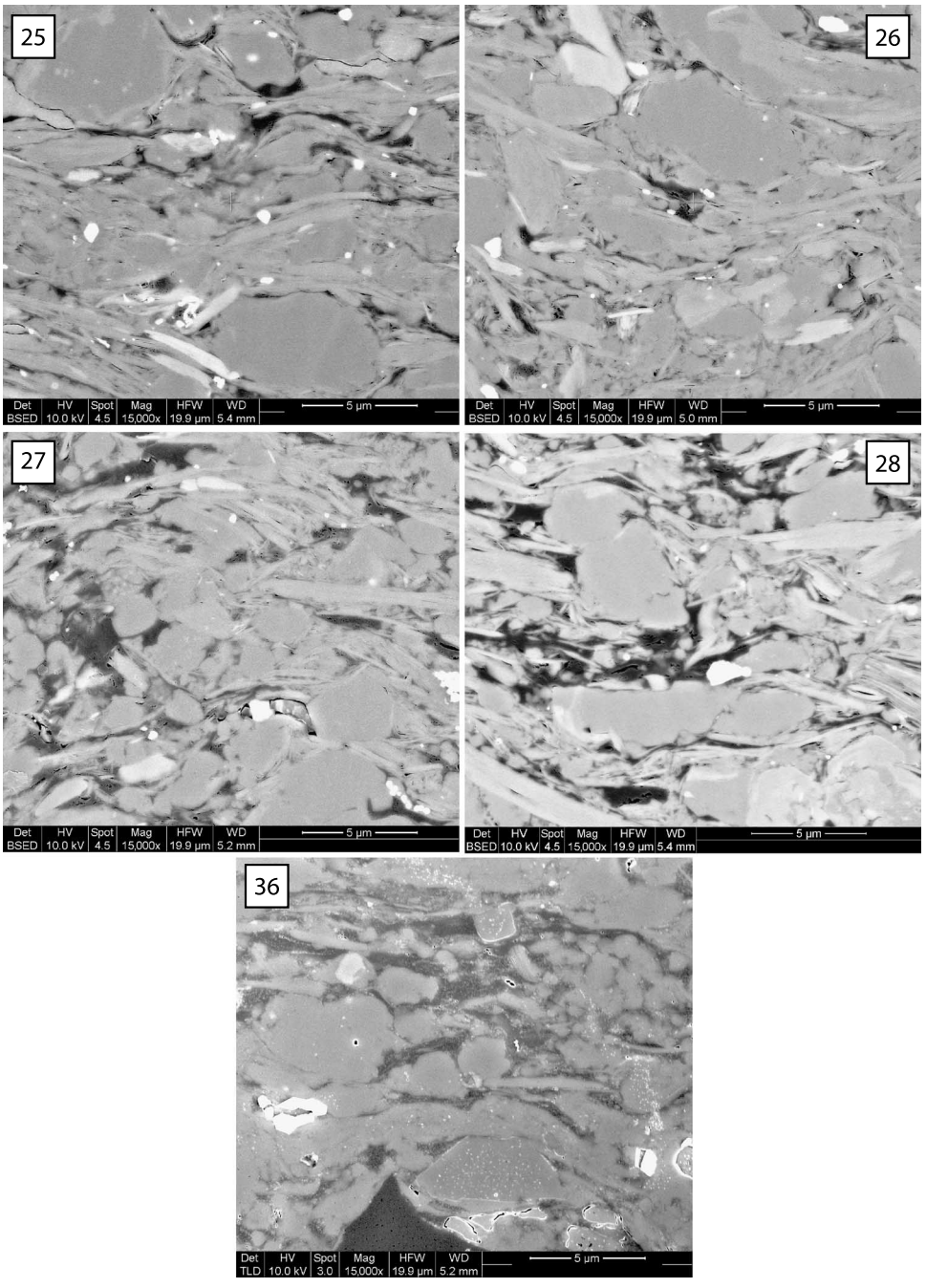

Figure 5. Backscattered electron images of samples from the higher maturity well. The numbers in image corners correlate to the sample numbers in Tables 1 and 2. Overall, the samples are dominated by siliciclastic grains of quartz and feldspar (equant) and micas (elongate). Darkest regions of images are mostly organic matter; brightest regions (white) are pyrite. Det BSED = backscattered electron detector; Det TLD = through the lens detector; HV = accelerating voltage; Spot = qualitative measure of beam current; WD= working distance; Mag = machine magnification; HFW = horizontal field width.

declines markedly with increasing TOC (Figures 13, 14). The four most TOC-rich samples in well 1 contain pore populations with distinctly fewer big pores (Figures 13, 14) and smaller median pore size (Figure 14A). Even apart from these four distinctively low-porosity samples, TOC and pore size manifest a generally tight and negative correlation across the entire sample set (Figure 14B).

Pore-size trends are complicated only by samples 1 to 15 in the lower maturity set and samples 2 to 28 in the high-maturity set. Samples 1 to 15 are relatively carbonate rich (Figure 13) (Table 2) and somewhat coarser grained than the other low-maturity samples. The pore-size distribution of this lower TOC sample contrasts from the size distributions in other lower TOC samples, primarily in terms of the lack of the larger end of the pore-size distribution (>120 nm). One possibility is that greater compaction related to pressure dissolution of carbonate grains has reduced the size of the

Table 1. Pore Measurements

Well	Sample	Depth (ft)	TOC (wt. %)*	TOC (BV %)*	Porosity (% BV)*	Φ_{om}*	$\Phi_{om\ bulk}$*	Φ_{min}*	Φ_{invis}*	Φ_{invis}/Φ_{tot}*	*n**	Avg Diam*	Std Dev*	Max*	Min*	D10*	D50*	D90*
1	15	5021	2.3	4.3	6.6	16.6	0.71	1.4	4.5	68.0	1478	37.2	29.1	327	7.8	84	39.8	20.5
1	18	5029	5.1	9.3	9.7	30.9	2.88	0.0	6.8	70.2	3246	30.9	36.5	784	6.6	465	82.5	18.8
1	22	5036	6.0	11.0	6.8	16.6	1.83	0.0	4.9	73.0	4209	27.5	22.5	415	5.8	154	36.8	16.6
1	27	5054	3.2	5.9	7.0	21.9	1.30	1.6	4.1	58.5	885	37.7	55.3	675	7.8	369	134.5	27.0
1	30	5062	3.8	7.0	7.5	22.5	1.58	0.8	5.1	68.4	1213	31.2	54.7	1123	3.9	453**	109.5	24.7
1	31	5064	8.1	14.6	6.7	3.03	0.44	0.0	6.3	93.4	2952	14.3	10.4	192	4.1	62	17.5	8.2
1	32	5066	10.2	18.3	7.3	1.60	0.29	0.0	7.0	96.0	2681	11.9	6.6	80	3.9	24	13.4	7.7
1	34	5071	12.8	22.6	6.4	0.6	0.13	0.0	6.3	98.0	1512	11.5	8.3	159	3.9	43	11.9	7.2
1	38	5083	13.6	24.3	5.5	0.4	0.10	0.0	5.4	98.2	612	13.1	11.2	264	5.5	149**	13.8	9.4
					Low TOC*	22	1.7	0.8	5.1	68		33	40	665	6	268	81	22
					High TOC*	1	0.2	0.0	6.2	96		13	9	174	4	43	14	8
2	25	9246	3.4	5.9	5.0	11.7	0.69	0.4	3.9	78.3	1919	29.8	37.8	568	5.2	185.6	56.2	15.9
2	26	9266	3.1	4.8	4.5	11.0	0.53	0.0	4.0	88.2	820	42.7	51.7	556	3.9	234.7	73.4	24.9
2	27	9272	6.4	10.5	8.0	7.5	0.79	0.0	7.2	90.2	1380	33.9	34.5	433	3.9	126.9	49.1	19.0
2	28	9278	8.3	13.0	8.7	10.8	1.41	0.0	7.3	83.8	1553	36.5	50.7	507	4.4	196.1	90.8	23.5
2	36	9302	10.7	16.1	8.6	7.3	1.17	0.0	7.4	86.4	3544	24.2	18.4	420	6.3	78.3	24.5	14.5
						10	0.9	0.1	6.0	85	28,004	33	39	497	5	164	59	20

*TOC (wt. %) = total organic carbon (wt. %); TOC (BV %) = total organic carbon (bulk volume percent); Porosity (% BV) = helium porosity (bulk volume percent); Φ_{om} = percentage of scanning electron microscopy–visible porosity within organic matter; $\Phi_{om\ bulk}$ = percentage of organic matter–hosted porosity in the bulk rock; Φ_{min} = percentage of mineral-hosted porosity in the bulk rock; Φ_{invis} = percentage of total porosity that is not captured by the imaging determination (Porosity [% BV] – $\Phi_{om\ bulk}$ – Φ_{min}); Φ_{invis}/Φ_{tot} = porosity that is below detection by imaging/bulk porosity; *n* = number of pores measured; Avg Diam = average diameter of pores based on measurement of long axes; Std Dev = standard deviation of the pore diameters measured as long axes; Max = largest pore diameter, measured as equivalent spherical diameter; Min = smallest pore diameter, measured as equivalent spherical diameter; D10 = pore diameter for which 10% of the total pores (by area) are larger; D50 = pore diameter for which 50% of the total pores (by area) are larger, the median diameter; D90 = pore diameter for which 90% of the total pores (by area) are larger. Low TOC = average for five lowest total organic carbon samples; High TOC = average for four highest total organic carbon samples.

**Samples for which the D10 value was exceeded by a single pore. The size of the largest pore is listed, expressed in equivalent circular diameter.

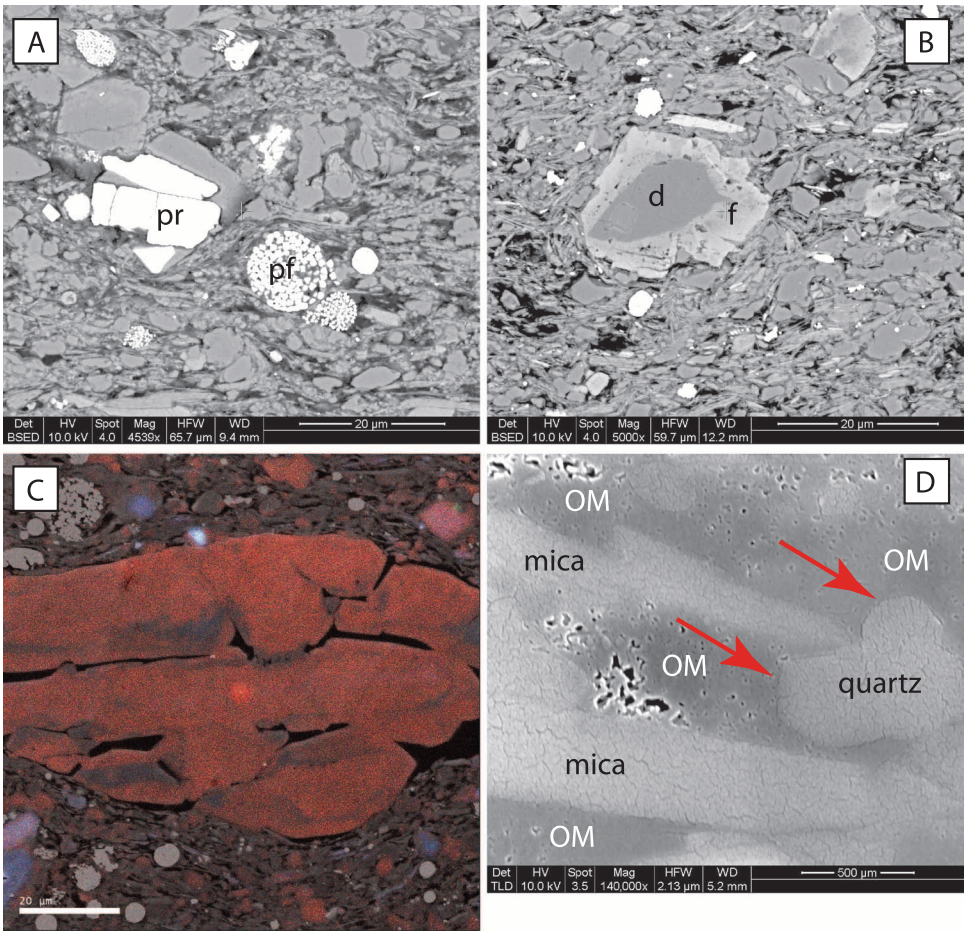

Figure 6. Authigenic components in Marcellus mudrocks. Det BSED = backscattered electron detector; Det TLD = through the lens detector; HV = accelerating voltage; Spot = qualitative measure of beam current; WD= working distance; Mag = machine magnification; HFW = horizontal field width. (A) Pyrite as euhedral grain replacement (pr) and framboids (pf). Sample 36. Backscattered electron image. (B) Ferroan dolomite (f) nucleated on a non–ferroan dolomite silt particle (d). Sample 27. Backscattered electron image. (C) Authigenic quartz with dull red and brownish luminescence replacing a fossil fragment (as interpreted from light microscopy). Sample 28. Mixed secondary-electron and cathodoluminescence image. (D) Euhedral borders on quartz crystals (arrows), surrounded by organic matter (OM). Other mineral grains are micas. Sample 36. Secondary electron image with a backscattered electron component.

intergrain spaces in this sample (Figure 4), limiting the size of the OM-hosted pores that must necessarily be confined within those spaces. Samples 2 to 28 in the high-maturity sample set are unique in having relatively abundant and large pores despite its moderately high TOC content (13 vol. %). No textural or composition factors that could explain this anomalous sample have been identified.

Pore-size distributions examined in probability density plots (pore number data) provide a useful visual display of the overall similarity of pore-size distribution across thermal maturity and the prominent changes in the pore population with increasing TOC (Figure 15). In samples with high TOC, a reduction in the maximum pore size (reduced right-side tail on the distribution) and a concentration of the pore population at a strong mode around 8 nm (apparent) exist (Figure 15C).

Given the polymodal character of the aggregated pore sizes suggested in the distributions presented in Figure 15, correspondence to a particular statistical distribution (for example, a log-normal distribution) cannot be fully assessed. Size distributions plotted for the pore types defined in Figure 3 demonstrate that, indeed, distinct subsets of pores of possibly contrasting genetic origins mixed in the overall pore populations exist (Figure 16). The four highest TOC samples in the lower maturity well have overall smaller modal sizes for each pore type. Isolated equant pores and discrete spongelike pores in the lower TOC samples have nearly identical distributions in the two wells. For complex and mineral-associated pores, the lower TOC samples in the lower maturity well have a lower modal pore size by pore number despite having a greater median size by pore area (cf. Figure 16 with Table 1). Analysis of pore-size distributions using Easy Fit®, a statistical package for distribution fitting, shows that most of the distributions presented in Figure 16 are described most precisely by a family of log-logistic distributions, similar to a log-normal distribution but with heavier right-side tails. This

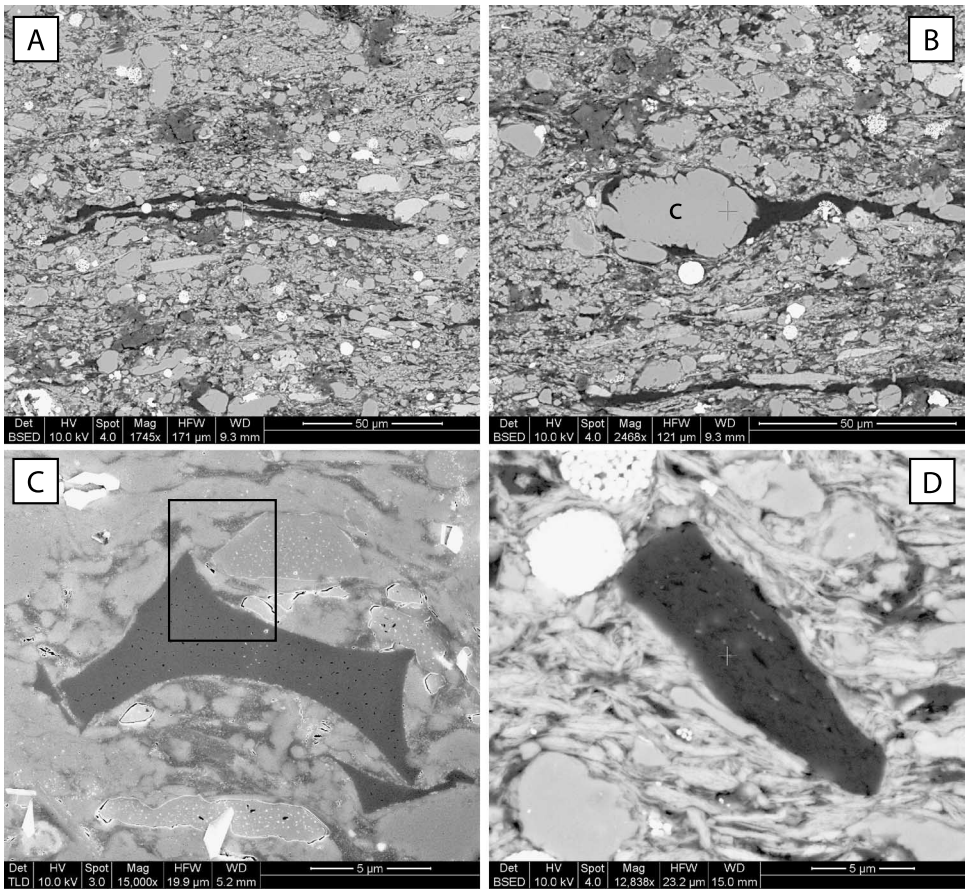

Figure 7. Particulate organic matter. Det BSED = backscattered electron detector; HV = accelerating voltage; Spot = qualitative measure of beam current; WD= working distance; Mag = machine magnification; HFW = horizontal field width. (A) Collapsed spore. Sample 36. Backscattered electron image. (B) Spore that was partially filled by calcite (c) before compaction. Sample 36. Backscattered electron image. (C) Probable wood fragment displaying arcuate edges representing former cell walls. The rectangle indicates the region that is enlarged in Figure 8A. Sample 36. Secondary electron image with a backscattered electron component. (D) Particulate organic matter of uncertain origin. This grain has minor pores and other textural and compositional inhomogeneity. Sample 28. Backscattered electron image.

distribution likely represents an artifact of the resolution of the SEM imaging and the attendant detection limit. Below 8 nm, the data are censored; no measurements below 4 nm were obtained. The use of a conductive coating adds uncertainty to the detection of very small pores because the coating may not be uniform across the surface of the sample or across different samples as a consequence of nonuniform electrostatic surface properties. An actual mode below 8 nm cannot be ruled out and, in fact, seems probable given the abundance of pores below the detection limit.

DISCUSSION

Overall Trends

A positive covariation between OM and bulk porosity has been noted previously in gas shales (Passey et al., 2010; Milliken et al., 2012a) and is unsurprising given the qualitative character of the observed pore distribution at the microscale in many organic-rich rocks (Loucks et al., 2009; Ambrose et al., 2010; Passey et al., 2010; Schieber, 2010; Sondergeld et al., 2010b; Curtis et al., 2011a; Curtis et al., 2011b; Milliken et al., 2012a). Given the pore-generating potential of the volume loss associated with OM devolatilizaton during maturation, it is unexpected to find that, even in the presence of an overall positive trend between TOC and bulk porosity (Figure 11), detectable pores in these Marcellus mudrocks (1) do not manifest strong trends in size or abundance across an increase in R_o from 1.0 to 2.1% (similar to the findings for two Marcellus Formation samples at R_o values of 1.1 and greater than 3.0% reported by Curtis et al. (2011c); (2) decline in volumetric abundance within the OM with increasing TOC; and (3) decline in size with increasing TOC; and (4) are mostly below the size of imaging by FE-SEM and especially so (>90%) in the highest TOC samples.

The dominance of pores of very small size (sub–5 nm) within OM has been noted in other

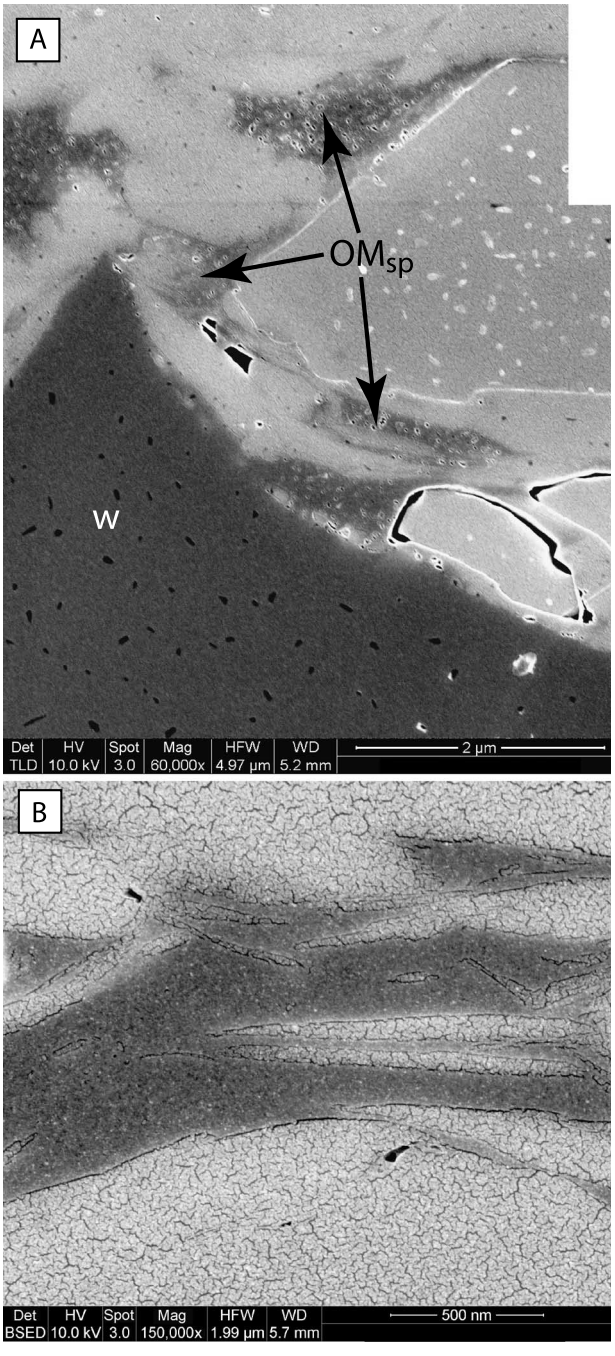

Figure 8. Probable solid bitumen. Det BSED = backscattered electron detector; Det TLD = through the lens detector; HV = accelerating voltage; Spot = qualitative measure of beam current; WD = working distance; Mag = machine magnification; HFW = horizontal field width. (A) Organic matter with spongelike pores (OM_{sp}) fills intergranular spaces uniformly. The porous structure of this distributed OM is distinct from that observed within the wood fragment (w). Area enlarged from Figure 7C. Sample 36. Secondary electron image with a backscattered electron component. (B) Extremely homogeneous texture and distribution of OM within intermineral spaces. Sample 38. Secondary electron image with a backscatter electron component.

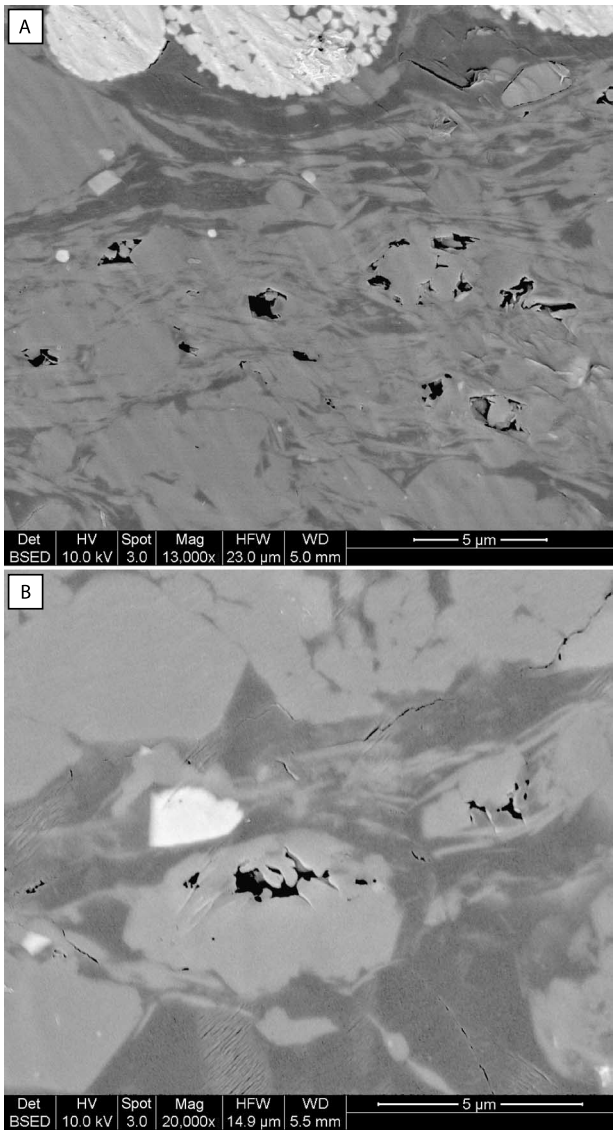

Figure 9. Sample treated with dichloromethane following argon-ion milling. Sample 1 to 34. Det BSED = backscattered electron detector; HV = accelerating voltage; Spot = qualitative measure of beam current; WD= working distance; Mag = machine magnification; HFW = horizontal field width. (A) Pores are dominantly mineral associated, and the organic matter (OM) appears unaffected by the solvent. (B) Dispersed and texturally homogenous OM appears unaffected by exposure to the solvent.

studies (Sondergeld et al., 2010a) and conforms to observations reported in coalbed methane studies (Beliveau, 1993; Bustin and Clarkson, 1998; Radlinski et al., 2004; Chalmers and Bustin, 2007), which, interestingly, also show a general lack of correlation between pore abundance and character and thermal maturity and a better correlation with OM type (Bustin and Clarkson, 1998).

Figure 10. Linear groupings of mineral-associated pores. The group at the upper center, left side (oval) is clearly associated with a mineral surface. The group at the center, right side (oval) is distant from a mineral surface but aligned parallel to the mineral material that crops out at the sample surface (arrows). The group at the lower right side (oval) is strongly linear, but the association with mineral surfaces is unclear. Secondary electron image of an argon-ion milled surface; has a substantial backscattered electron component. Det TLD = through the lens detector; HV = accelerating voltage; Spot = qualitative measure of beam current; WD = working distance; Mag = machine magnification; HFW = horizontal field width.

Organic Matter Type

The foregoing observations raise compelling questions about the nature of OM in the Marcellus and the possible control of OM type on the evolution of OM-hosted pore systems. Small-scale spatial heterogeneity in OM-hosted porosity has been noted at the nanometer to micrometer scale in previous studies (Loucks et al., 2009; Curtis et al., 2011b) as well as here (contrast, for example, the pores within particulate versus pore-filling OM in the upper image of Figure 8) and is a strong indication that OM type (kerogens of marine or terrestrial origin, or solid bitumen) is likely an important control on pore formation. The trends observed in this study raise the question of whether variation in the bulk composition of OM has an impact on the pore-size distribution of the OM-hosted pore system.

Description of OM type via light microscopy, particularly reflected light microscopy, has been a standard practice for many decades (e.g., Stach et al., 1982; Taylor et al., 1998). By contrast, petrographic criteria for the identification of OM type using SEM imaging remain poorly defined. Methods for the assessment of OM compositional variation at high spatial resolution offer possible solutions (e.g., Bernard et al., 2010a, b; Keleman et al., 2010) but have not yet been widely applied.

A challenge relates to the established practice of defining certain OM types based on chemical instead of petrographic criteria. From a chemical standpoint, kerogen is defined as OM "that is soluble neither in aqueous alkaline solvents nor in the common organic solvents" (Tissot and Welte, 1984, p. 131). By contrast, bitumen is defined, chemically, as a material that is soluble (Tissot and Welte, 1984). The overall lack of OM mobilization by dichloromethane in this study (Figure 9) supports the interpretation of this OM as a kerogen or, alternatively, solid bitumen, a finding that accords with the stability of the material under vacuum and electron beam bombardment.

The chemical definition of OM type only partially overlaps a petrography-based definition, whereby kerogen is generally understood to be

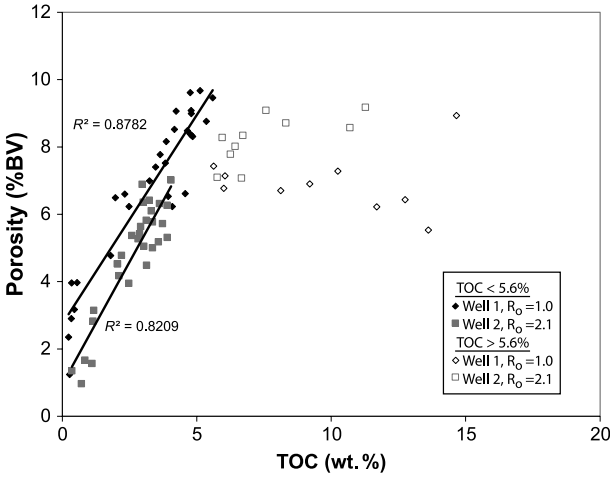

Figure 11. Total organic carbon (TOC, wt. %) versus measured bulk porosity (bulk volume percent [% BV] by tight rock analysis [TRA] method as described in the methods section) in two wells of contrasting thermal maturity. Total organic carbon (TOC) values below 5.6 wt. % display a positive covariation with bulk porosity (R^2 values shown). Above a TOC value of 5.6 wt. % (open symbols), this covariation disappears in the lower maturity well and is diminished in the higher maturity well. R_o = vitrinite reflectance.

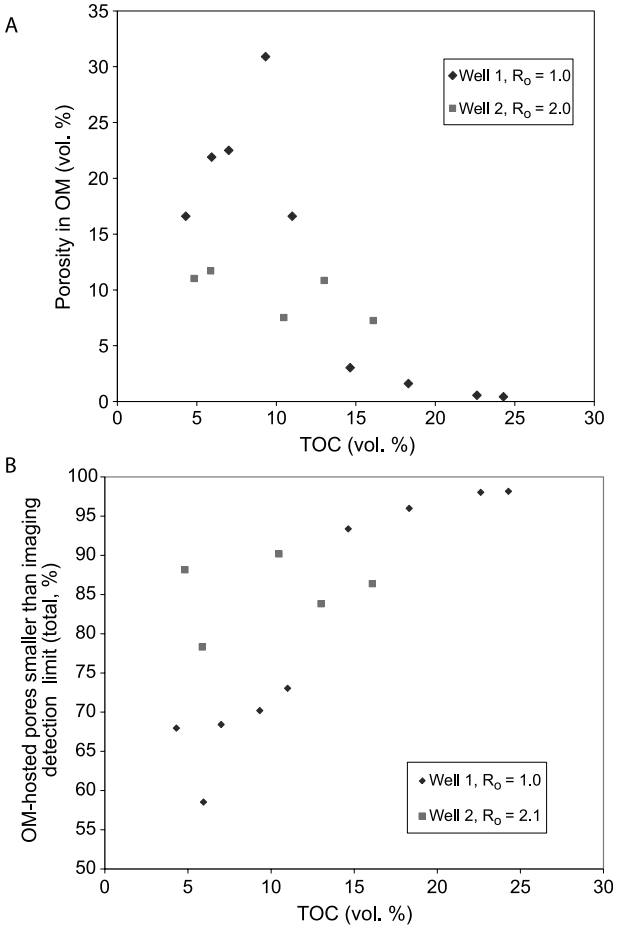

Figure 12. Trends between total organic carbon (TOC) and porosity values determined by imaging. (A) TOC (vol. %) versus porosity within organic matter (OM). (B) TOC (vol. %) versus the percent of the bulk volume porosity that was not accounted for by pores (mineral- and OM-hosted) observed and measured from images. R_o = vitrinite reflectance.

affiliated with particulate OM, either terrigenous or marine, whereas bitumen is a liquid, or a former liquid, hydrocarbon released into pores during kerogen maturation. Teerman et al. (1995) have emphasized the need for a standardized terminology that can be applied to petrographically unstructured OM and noted the difficulties in discriminating weakly or cryptically structured kerogens (amorphinite) of either marine (alginite) or terrigenous (bituminite) origin from solid bitumens (Teerman et al., 1995, p. 15–16, 21). A transmission electron microscope observation of bituminite (Taylor et al., 1991) reveals faint intraparticle structures that would, theoretically, be detectable at the scales of observation applied here but are not observed. A key gap in petrographic understanding relates to the appearance of diagenetically altered marine kerogen, a material that is potentially more labile and deformable by compaction than the terrigenous kerogens (spores and wood) that are clearly identifiable in the Marcellus samples. An interpretation of the uniformly distributed structureless OM as marine kerogen that has been extremely deformed by compaction or, alternatively, absorbed or otherwise intimately admixed with clays at the time of deposition (Kennedy et al., 2002) cannot be strictly ruled out.

Solid bitumen, also called "pyrobitumen," "migrabitumen," "dead oil," and a variety of other terms (Landis and Castano, 1995), represents a possible alternative interpretation for the homogeneous, unstructured, and dispersed OM. Spatial distribution that engulfs detrital grains has been cited as evidence for solid bitumen (Thompson-Rizer, 1987; Jacob, 1989), an observation that is consistent with the petrographic appearance of the homogenous OM in this study. However, the occurrence of solid bitumen is somewhat incongruous with the low maturity of well 1 (R_o = 1.0%). Low-temperature solid bitumens, variously known as "wurtzilite," "albertite," and "grahamite" (Jacob, 1989; Tannenbaum and Aizenshtat, 1984), have been noted where certain high-productivity marine environments produce marine kerogen that is sulfur rich (Powell et al., 1975; Tannenbaum and Aizenshtat, 1985; Orr, 1986). Sulfur linkages within the organic compounds (Orr, 1986; Baskin and Peters, 1992) yield insoluble bitumens that are solid at R_o values as low as 0.5% (Jacob, 1989, his figure 11, p. 77). Compositional analysis of the OM is beyond the scope of our study, but the potential for the sulfide-rich Marcellus to host such immature solid bitumen seems plausible. Resolving the uncertainty surrounding the petrographic character versus the composition of the OM (kerogen versus bitumen) would contribute importantly to our understanding of the spatial distribution of OM-hosted pore systems.

If OM type is a factor in the evolution of OM-hosted pores, then it becomes plausible to also associate pore character with depositional environment. The stratigraphic position of the most TOC-rich

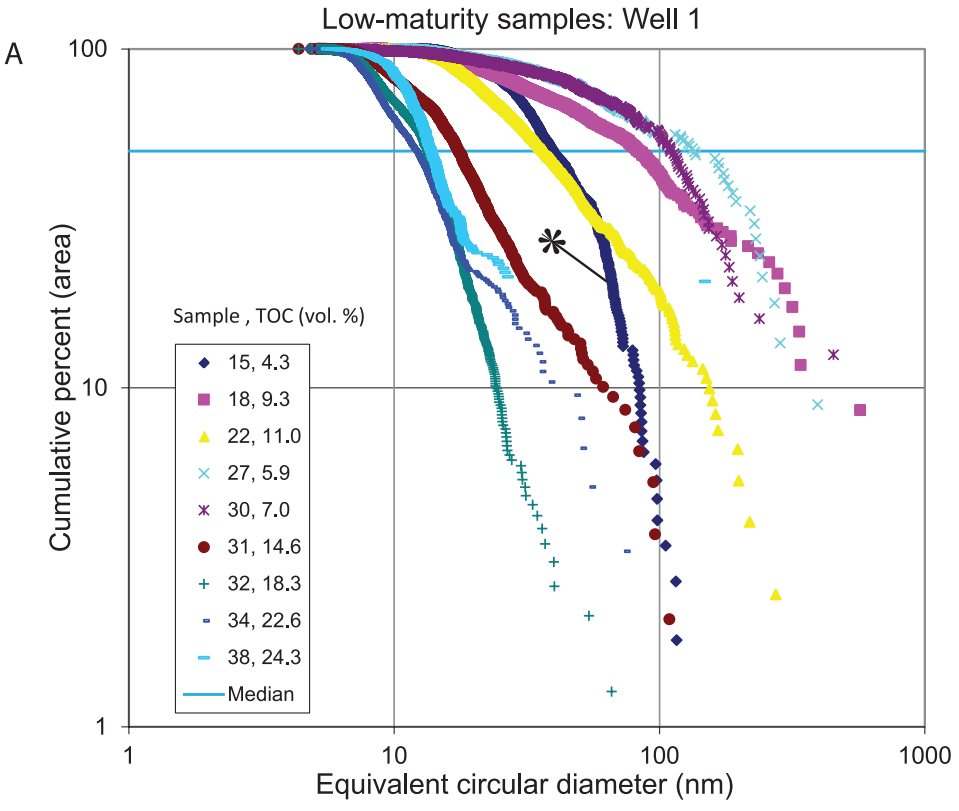

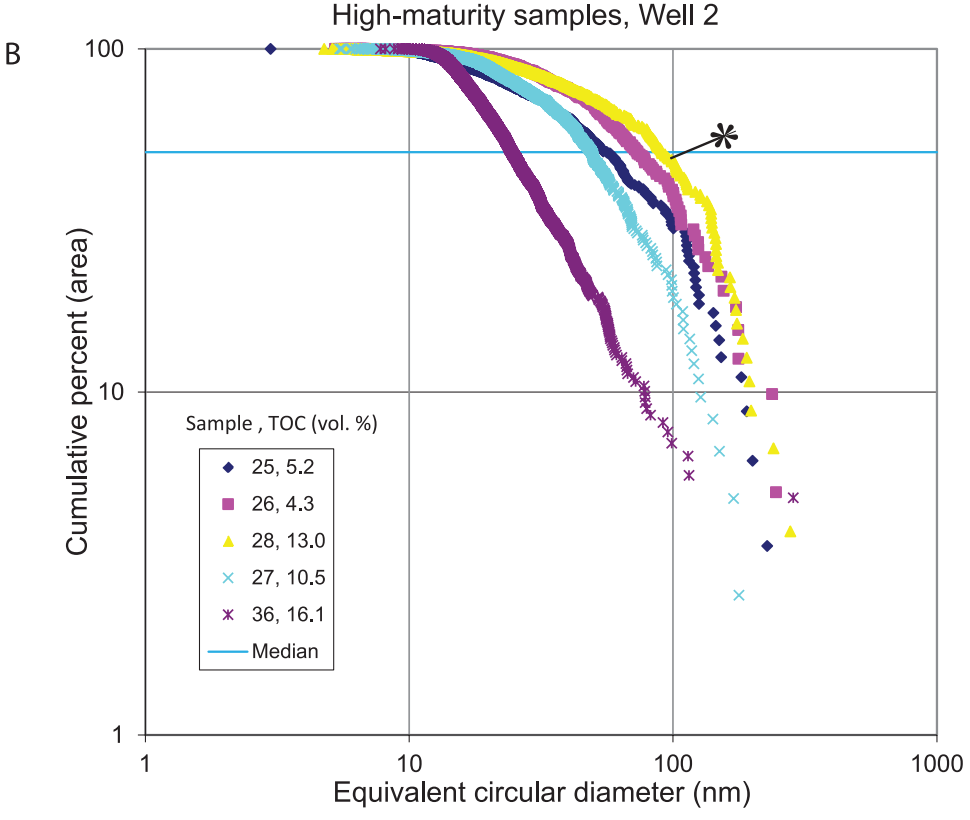

Figure 13. Pore-size distributions (based on pore area, a proxy for volume) for low-maturity sample set (vitrinite reflectance [R_o] =1.0%) (A) and high-maturity sample set (R_o = 2.1%) (B). In each plot, a single anomalous sample is indicated (*), which does not follow the overall trends as documented in Figure 14. See text for further discussion. One large pore comprising approximately 20% of the total pore area is omitted from the distribution of Sample 38 in the low-maturity set. The horizontal blue line marks the 50th percentile (median pore diameter). TOC = total organic carbon.

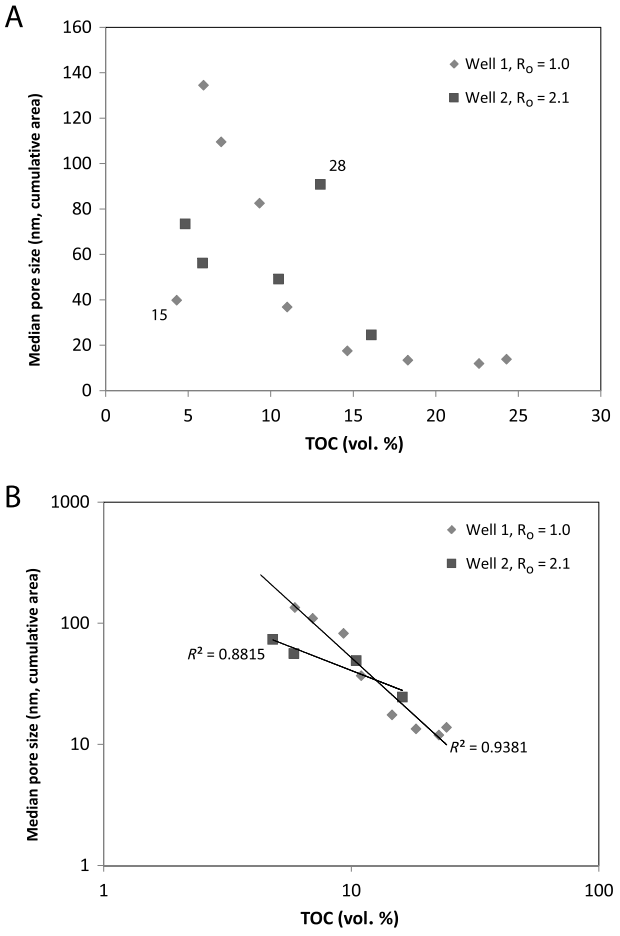

Figure 14. Total organic carbon (TOC; vol. %) versus the median pore diameter (based on cumulative pore area). (A) Entire data set. Two anomalous samples are labeled: 15 in the low-maturity set has fewer and smaller pores than other samples of similar organic matter content; 28 in the high-maturity set has more and larger pores than expected based on other samples of similar TOC. (B) Correlations with two anomalous samples removed from the data set. See text for discussion. R_o = vitrinite reflectance.

samples in proximity to a maximum flooding surface (high gamma-ray response) in the lowermost Marcellus (Lash and Engelder, 2011) is consistent with a kerogen of dominantly marine composition with attendant implications for local generation of abundant bitumen.

Implications for Free Versus Adsorbed Gas

Ambrose et al. (2010) point out that, at pore sizes below 50 nm, absorption of methane on pore walls (relative to free gas that is more mobile within the pore) becomes significant and, at sizes below 10 nm, becomes a very strong effect. This study demonstrates that the pores of sufficient size to host a substantial part of free gas are within the range of measurement by FE-SEM imaging and, in fact, the transition to pores sufficiently small to host dominantly adsorbed gas is near the detection limit for pore imaging by FE-SEM. Also clear is that a significant part of the total OM-hosted pores in all of the samples examined here and especially in the most organic-rich samples (Figure 13B) are sufficiently small (below the detection limit for imaging) that they are expected to contain dominantly adsorbed gas.

Gas Generation and Expulsion

The presence of a relatively continuous OM matrix has important implications for hydrocarbon expulsion pathways in a rock that generally lacks a significant interparticle pore system (Hover et al., 1996). In the two-dimensional data collected here, the three-dimensional connectivity of the OM and the OM-hosted pores is uncertain, although images of the higher TOC samples (approaching 25 vol. % OM) at least give the qualitative impression of a potentially continuous organic matrix (Figures 4, 5, 8B; samples 34 and 36).

The contrasting distribution of different OM-hosted pore types within OM, as well as the polymodal pore-size distributions observed, opens the possibility that pores have formed by more than one mechanism. Larger pores localized on mineral surfaces (mineral-associated pores; Figures 10, 11) suggest a possible interpretation as voids formed by heterogeneous nucleation of methane bubbles, an interpretation that would further tend to support the bitumen interpretation of the OM, although bubble growth within a very soft kerogen might also be possible. The clustering and spatial affiliation of the mineral-associated, complex, and discrete spongelike pores suggest that these pore types may be part of a continuum of pores of a range of size, all related to nucleation in association with mineral surfaces. Preferred nucleation of pores (former bubbles) on mineral surfaces is consistent with the experimental observation that clay minerals preferentially catalyze gas formation over

Table 2. Bulk Rock Composition

Well	Sample	Depth	Porosity	Permeability	TOC* (wt. %)	TOC (vol. %)	Quartz	K-Feldspar	Plagioclase	Calcite	Siderite	Ankerite/Ferrous Dolomite	Dolomite	Pyrite	Fluorapatite	Barite	Illite/Smectite (I/S)	Illite + Mica	Kaolinite	Chlorite
1	15	5021.2	6.60	0.000351	2.3	4.3	26.8	4.79	1.00	17.82	0.00	0.09	1.83	1.64	0.00	0.41	14.4	24.2	0.00	3.77
1	18	2058.7	9.67	0.000446	5.1	9.3	24.8	6.23	2.10	1.09	0.00	0.33	1.17	4.46	0.00	0.22	15.3	33.0	1.25	2.81
1	22	5036.2	6.77	0.000349	6.0	11.0	22.8	5.34	1.71	9.80	0.00	0.00	2.16	7.88	0.00	0.06	11.5	27.7	0.38	2.36
1	27	5053.9	6.99	0.000329	3.2	5.9	27.9	6.09	2.94	1.68	0.13	0.00	2.65	4.17	0.00	0.00	11.5	35.0	0.59	2.70
1	30	5061.6	7.52	0.000458	3.8	7.0	30.1	3.57	3.40	1.02	0.00	0.42	1.87	5.26	0.00	0.11	11.0	35.4	0.49	1.97
1	31	5064.3	6.70	0.000460	8.1	14.6	28.5	7.01	3.30	3.14	0.00	0.00	1.84	6.98	0.00	0.05	12.0	25.3	0.00	0.67
1	32	5065.7	7.28	0.000486	10.2	18.3	30.7	7.42	2.93	0.76	0.00	0.00	1.63	8.14	0.00	0.05	10.9	22.4	0.00	0.82
1	34	5071.2	6.43	0.000401	12.8	22.6	23.1	10.65	2.66	2.86	0.00	0.00	3.29	8.84	0.00	0.00	10.8	20.2	0.00	0.00
1	38	5082.7	5.53	0.000352	13.6	24.3	19.6	4.35	5.63	6.58	0.00	0.00	3.95	10.4	0.00	0.40	7.4	22.9	0.00	0.00
2	25	9245.9	5.82	0.000310	3.4	5.2	33.6	8.02	3.89	1.33	0.00	2.09	0.00	2.84	0.00	0.06	13.8	25.8	0.00	5.31
2	26	9265.9	5.20	0.000210	3.1	4.8	35.4	2.03	7.95	5.49	0.00	0.00	2.61	2.14	0.08	0.06	13.5	22.6	0.00	4.57
2	27	9272.2	8.82	0.000587	6.4	10.5	32.7	5.51	3.77	1.65	0.00	0.00	1.87	8.43	0.00	0.83	10.5	26.7	0.21	2.53
2	28	9278.5	9.49	0.000749	8.3	13.0	30.9	7.62	4.70	3.56	0.00	0.00	3.77	5.08	0.00	0.39	13.0	21.0	0.00	1.15
2	36	9302.4	9.12	0.000624	10.7	16.1	44.4	8.69	2.96	2.82	0.00	0.00	3.21	2.67	0.00	0.00	6.0	16.0	0.00	0.25

*TOC = total organic carbon.

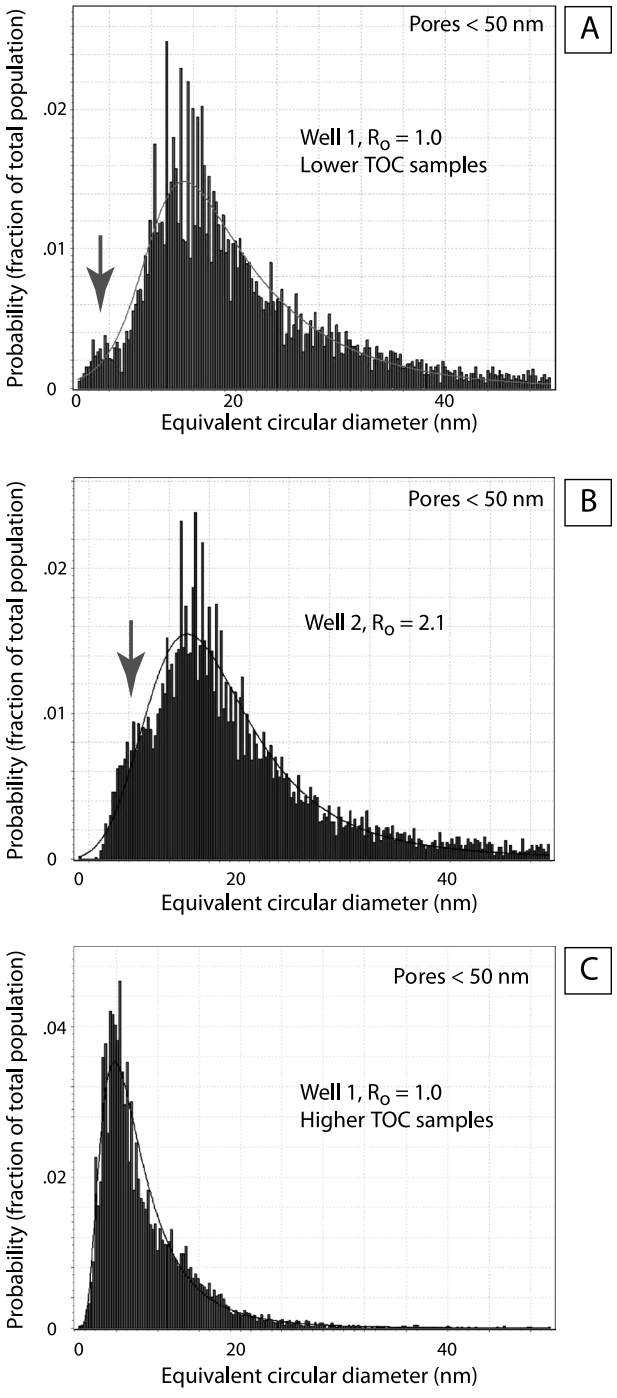

Figure 15. Probability density plots of pore size (limited to pores <50-nm equivalent circular diameter). The arrows indicate possible subpopulation modes around 8 nm, a mode that becomes dominant in the higher TOC samples. TOC = total organic carbon; R_o = vitrinite reflectance.

other forms of hydrocarbon during maturation (Tannenbaum et al., 1986). The petrographic observations we report here, in fact, suggest that the mechanism of catalysis involves the presence of sites favorable to the nucleation of gas bubbles on phyllosilicate mineral surfaces, which are very abundant in the Marcellus Formation mudrocks.

The isolated equant pores are distributed more uniformly through the OM and may form by a different mechanism, possibly by homogeneous bubble nucleation. Alternatively, these smallest pores may represent a residual population, left behind during gas expulsion, because frictional forces on the bubble walls were too great for them to move in viscous bitumen (Brown, 2000).

We have already suggested that the relationships between sample TOC and visible SEM porosity documented in this article may be influenced by OM type, but this does not preclude other processes. Samples with higher TOCs and the lowest OM porosities may represent rocks in which the gas expulsion process was more complete as a consequence of greater OM connectivity and OM compactability, whereas samples with higher OM porosities (lower TOCs) may represent situations in which rigid mineral frameworks inhibited compactional expulsion of the methane-filled bubbles. These latter samples may represent rocks that retain a greater proportion of their generated gas in the form of free gas as opposed to absorbed gas. If the foregoing interpretations are correct, the size distributions of OM pores (former bubbles) may preserve information on the dual mechanisms of gas generation and gas expulsion. A fuller understanding of the chemical/mechanical processes recorded by OM-hosted pores awaits further statistical analysis of the pore-size distributions and, possibly, experimental work on pore generation during maturation. Clearly, prediction of OM-hosted pore systems will depend not only on an understanding of OM type, but also on bulk rock composition and texture. Both chemical (maturation) and mechanical (compactional) processes may be factors in the creation, preservation, and destruction of OM-hosted pores.

CONCLUSIONS

This study demonstrates the somewhat surprising result that pores hosted within OM do not manifest

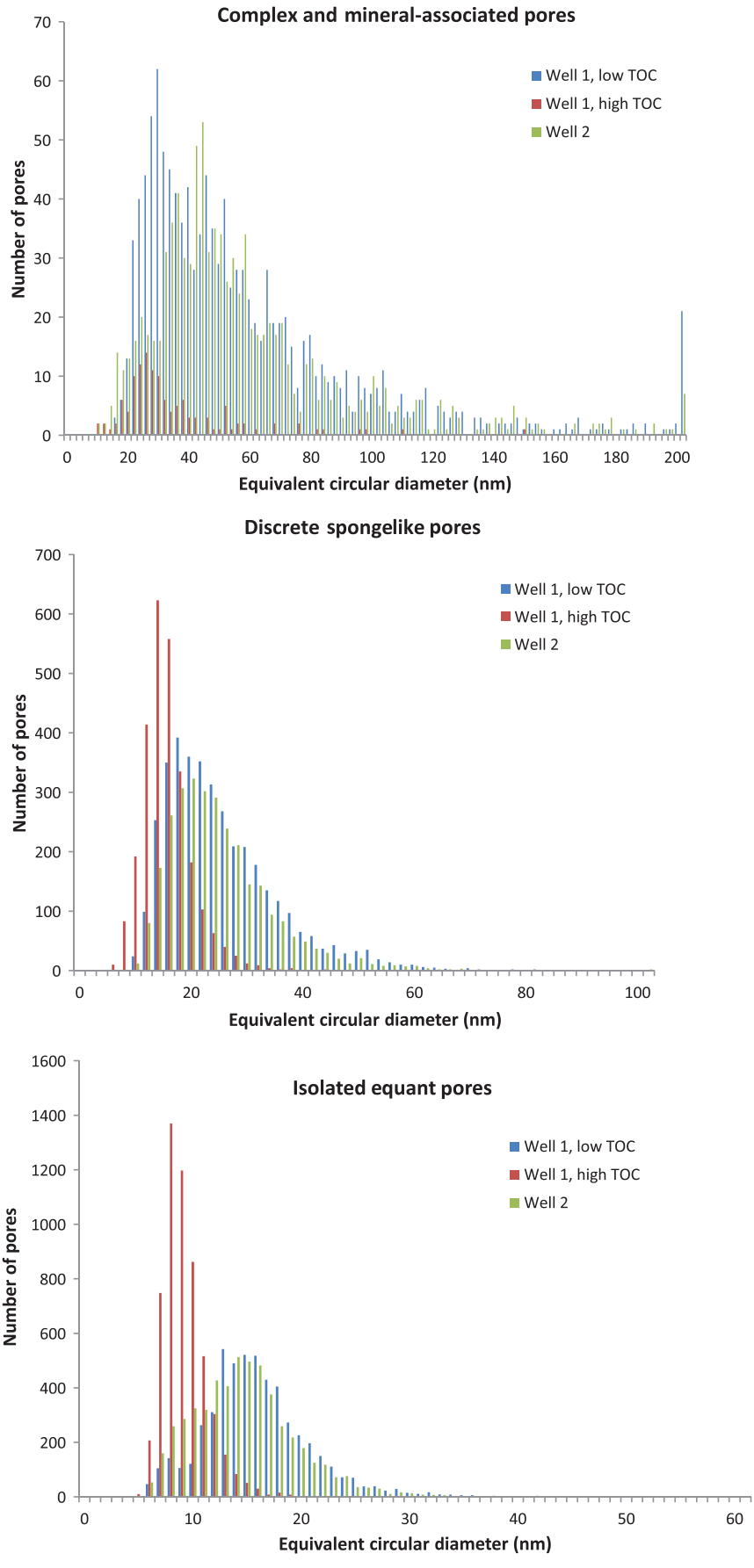

Figure 16. Pore-size distributions for the pore types defined in Figure 3. Plots are based on pore number.

change in abundance or type, which can be correlated with thermal maturity. At a thermal maturity between an R_o of 1.0 and 2.1% in the Marcellus Formation of northern Pennsylvania, variation of TOC is a stronger control on the character of OM-hosted pore systems than variation in thermal maturity. Although TOC shows an important correlation with porosity in many samples, that trend only holds at the lower end of the TOC range. Organic matter–hosted pores in highest TOC samples contain smaller pores and a larger fraction of pores that are below the detection limit of imaging by FE-SEM. Particulate OM occurs in these rocks and, in many instances, can be clearly discriminated because of the presence of sharp edges and distinctive internal fabric. Much of the OM in all the samples and, especially, in the higher TOC samples, has petrographic characteristics that are consistent with solid bitumen that fills intergranular pores, but an origin as extremely ductile and structureless kerogen cannot be ruled out at this point. Results of this study provide motivation for additional work on porosity evolution at lower maturity and for an improved understanding of OM petrography in the SEM.

REFERENCES CITED

Ambrose, R. J., R. C. Hartman, M. Dias-Campos, Y. Akkutlu, and C. H. Sondergeld, 2010, New pore-scale considerations for shale gas in place calculations: Society of Petroleum Engineers Unconventional Gas Conference, Pittsburgh, Pennyslvania, February 23–25, 2010, SPE Paper 131772, 17 p., doi:10.2118/131772-MS.

Baskin, D. K., and K. E. Peters, 1992, Early generation characteristics of a sulfur-rich Monterey kerogen: AAPG Bulletin, v. 76, p. 1–13.

Beaumont, C., G. M. Quinlan, and J. Hamilton, 1987, The Alleghanian orogeny and its relationship to the evolution of the Eastern Interior, North America, *in* C. Beaumont and A. J. Tankard, eds., Sedimentary basins and basin-forming mechanisms:Canadian Society of Petroleum Geologists Memoir 12, p. 425–445.

Beliveau, D., 1993, Honey, I shrunk the pores! Journal of Canadian Petroleum Technology, v. 32, p. 15–17, doi:10.2118/93-08-01.

Bernard, S., O. Beyssac, K. Benzerara, N. Findling, G. Tzvetkov, and G. E. Brown, 2010a, XANES, Raman and XRD study of anthracene-based cokes and saccarose-based chars submitted to high-temperature pyrolysis: Carbon, v. 48, p. 2506–2506, doi:10.1016/j.carbon.2010.03.024.

Bernard, S., et al., 2010b, Multiscale detection of organic and inorganic signatures provides insights into gas shale properties and evolution: Chemie der Erde–Geochemistry, v. 70, p. 119–133, doi:10.1016/j.chemer.2010.05.005.

Brown, A., 2000, Evaluation of possible gas microseepage mechanisms: AAPG Bulletin, v. 84, p. 1775–1789.

Bustin, R. M., and C. R. Clarkson, 1998, Geological controls on coalbed methane reservoir capacity and gas content: International Journal of Coal Geology, v. 38, p. 3–26, doi:10.1016/S0166-5162(98)00030-5.

Chalmers, G., and R. M. Bustin, 2007, On the effects of petrographic composition on coalbed methane sorption: International Journal of Coal Geology, v. 69, p. 288–304, doi:10.1016/j.coal.2006.06.002.

Curtis, M., C. Sondergeld, R. Ambrose, and C. Rai, 2011a, Microstructural observations in gas shales: AAPG Search and Discovery article 90122, http://www.searchanddiscovery.com/documents/2011a/90122curtis/images/curtis.pdf (accessed July 30, 2012).

Curtis, M. E., R. Ambrose, C. Sondergeld, and C. Rai, 2011b, Transmission and scanning electron microscopy investigation of pore connectivity of gas shales on the nanoscale: Society of Petroleum Engineers North American Unconventional Gas Conference and Exhibition, The Woodlands, Texas, June 14–16, 2011, SPE Paper 144391, 10 p., doi:10.2118/144391-MS.

Curtis, M. E., R. J. Ambrose, C. H. Sondergeld, and C. S. Rai, 2011c, Investigation of the relationship between organic porosity and thermal maturity in the the Marcellus Shale: Society of Petroleum Engineers North American Unconventional Gas Conference and Exhibition, The Woodlands, Texas, June 14–16, 2011, SPE Paper 144370, 4 p., doi:10.2118/144370-MS.

Engelder, T., and G. G. Lash, 2008, Marcellus Shale play's vast resource potential creating stir in Appalachia: The American Oil & Gas Reporter, May 2008, p 77–78, 81–82, 85–87.

Ettensohn, F. R., 1985, The Catskill delta complex and the Acadian orogeny: A model, *in* D. L. Woodrow and W. D. Sevon, eds., The Catskill delta: Geological Society of America Special Paper 201, p. 39–49.

Evans, M. A., 1995, Fluid inclusions from the Middle Devonian shales: A record of deformation conditions and fluid evolution in the Appalachian Plateau: Geological Society of American Bulletin, v. 107, p. 327–339, doi:10.1130/0016-7606(1995)107<0327:FIIVFT>2.3.CO;2.

Gray, M. B., and J. Stamatakos, 1997, New model for evolution of fold and thrust belt curvature based on structural and paleomagnetic results from the Pennsylvania salient: Geology, v. 25, p. 1065–1070, doi:10.1130/0091-7613(1997)025<1067:NMFEOF>2.3.CO;2.

Handwerger, D. A., R. Suarez-Rivera, K. I. Vaughn, and J. F. Keller, 2011, Improved petrophysical core measurements on tight shale reservoirs using retort and crushed samples: Society of Petroleum Engineers Annual Technical Conference and Exhibition, Denver, Colorado, October 30–November 2, 20122, SPE Paper 147456, 21 p., doi:10.2118/147456-MS.

Hover, V. C., D. R. Peacor, and L. M. Walter, 1996, Relationship between organic matter and authigenic illite/smectite in Devonian black shales, Michigan and Illinois

basins, U.S.A., *in* L. J. Crossey, R. G. Loucks, and M. W. Totten, eds., Siliciclastic diagenesis and fluid flow: Concepts and applications: Society for Sedimentary Geology Special Publication 55, p. 73–83.

Jacob, H., 1989, Classification, structure, genesis and practical importance of natural solid oil bitumen ("migrabitumen"): International Journal of Coal Geology, v. 11, p. 65–79, doi:10.1016/0166-5162(89)90113-4.

Johnsson, M. J., 1986, Distribution of maximum burial temperatures across northern Appalachian Basin and implications for Carboniferous sedimentation patterns: Geology, v. 14, p. 384–387, doi:10.1130/0091-7613(1986)14<384:DOMBTA>2.0.CO;2.

Keleman, S. R., et al., 2010, Characterization of solid bitumens originating from thermal chemical alteration and thermochemical sulfate reduction: Geochimica et Cosmochimica Acta, v. 74, p. 5305–5332, doi:10.1016/j.gca.2010.06.013.

Kennedy, M. J., D. R. Pevear, and R. J. Hill, 2002, Mineral surface control of organic carbon in black shale: Science, v. 295, p. 657–660, doi:10.1126/science.1066611.

Landis, C. R., and J. R. Castano, 1995, Maturation and bulk chemical properties of a suite of solid hydrocarbons: Organic Geoochemistry, v. 22, p. 137–149, doi:10.1016/0146-6380(95)90013-6.

Lash, G. G., and T. Engelder, 2011, Thickness trends and sequence stratigraphy of the Middle Devonian Marcellus Formation, Appalachian Basin: Implications for Acadian foreland basin evolution: AAPG Bulletin, v. 95, p. 61–103, doi:10.1306/06301009150.

Laughrey, C. D., T. E. Ruble, H. Lemmens, J. Kostelnik, A. R. Butcher, G. Walker, and W. Knowles, 2011, Black shale diagenesis: Insights from integrated high-definition analyses of postmature Marcellus Formation rocks, northeastern Pennsylvania: http://www.gcpg.org/CSPG/Technical/Webcast_Archive (accessed June 27, 2012).

Loucks, R. G., R. M. Reed, S. C. Ruppel, and D. M. Jarvie, 2009, Morphology, genesis, and distribution of nanometer-scale pores in mudstones of the Mississippian Barnett Shale: Journal of Sedimentary Research, v. 79, p. 848–861, doi:10.2110/jsr.2009.092.

Loucks, R. G., R. M. Reed, S. C. Ruppel, and U. Hammes, 2012, Spectrum of pore types and networks in mudrocks and a descriptive classification for matrix-related mudrock pores: AAPG Bulletin, v. 96, p. 1071–1098, doi:10.1306/08171111061.

Luffel, D. L., F. K. Guidry, and J. B. Curtis, 1996, Development of laboratory and petrophysical techniques for evaluating shale reservoirs: Gas Research Institute Final Report GRI-95/0496 (October 1986–September 1993), p. 301.

Macquaker, J. H. S., and A. E. Adams, 2003, Maximizing information from fine-grained sedimentary rocks: An inclusive nomenclature for mudstones: Journal of Sedimentary Research, v. 73, p. 735–744, doi:10.1306/012203730735.

Milliken, K. L., W. L. Esch, R. M. Reed, and T. Zhang, 2012a, Grain assemblages and strong diagenetic overprinting in siliceous mudrocks, Barnett Shale (Mississippian), Fort Worth Basin, Texas, U.S.A.: AAPG Bulletin, v. 96, p. 1553–1578.

Milliken, K. L., P. K. Papazis, R. J. Day-Stirrat, and C. Dohse, 2012b, Carbonate lithologies of the Barnett Shale, *in* J. Breyer, ed., Shale reservoirs: Giant resources for the 21st century: AAPG Memoir 97, p. 290–321.

Orr, W. L., 1986, Kerogen/asphaltene/sulfur relationships in sulfur-rich Monterey oils: Organic Geochemistry, v. 10, p. 499–516, doi:10.1016/0146-6380(86)90049-5.

Passey, Q. R., K. M. Bohacs, W. L. Esch, R. Kimentidis, and S. Sinha, 2010, From oil-prone source rock to gas-producing shale reservoir: Geologic and petrophysical characterization in unconventional shale-gas reservoirs: Chinese Petroleum Society/Society of Petroleum Engineers International Oil & Gas Conference and Exhibition, Beijing, China, June 8–10, 2010, SPE Paper 121250, 29 p., doi:10.2118/131350-MS.

Powell, T. G., P. J. Cook, and D. M. McKirdy, 1975, Organic geochemistry of phosphorites: Relevance to petroleum genesis: AAPG Bulletin, v. 59, p. 618–632.

Radlinski, A. P., M. Mastalerz, A. L. Hinde, M. Hainbuchner, H. Rauch, M. Baron, J. S. Lin, L. Fan, and P. Thiyagarajan, 2004, Application of SAXS and SANS in evaluation of porosity, pore-size distribution and surface area of coal: International Journal of Coal Geology, v. 59, p. 245S–271, doi:10.1016/j.coal.2004.03.002.

Reed, J. S., J. A. Spotila, K. A. Eriksson, and R. J. Bodnar, 2005, Burial and exhumation history of Pennsylvanian strata, central Appalachian Basin: An integrated study: Basin Research, v. 17, p. 259–268, doi:10.1111/j.1365-2117.2005.00265.x.

Roden, M. K., and D. S. Miller, 1989, Apatite fission-track thermochronology of the Pennsylvania Appalachian Basin: Geomorphology, v. 2, p. 39–51, doi:10.1016/0169-555X(89)90005-6.

Roduit, N., 2008, JMICROVISION Version 1.2.7: Image analysis toolbox for measuring and quantifying components of high-definition images: http://www.jmicrovision.com (accessed November 15, 2006).

Schieber, J., 2010, Common themes in the formation and preservation of intrinsic porosity in shales and mudstones: Illustrated with examples from across the Phanerozoic: Society of Petroleum Engineers Unconventional Gas Conference, Pittsburgh, Pennsylvania, February 23–25, 2010, SPE Paper 132379, 10 p., doi:10.2118/132370-MS.

Slatt, R. M., and N. R. O'Brien, 2011, Pore types in the Barnett and Woodford gas shales: Contribution to understanding gas storage and migration pathways in fine-grained rocks: AAPG Bulletin, v. 95, p. 2017–2030, doi:10.1306/03301110145.

Sondergeld, C., K. E. Newsham, J. T. Comiski, M. C. Rice, and C. S. Rai, 2010a, Petrophysical considerations in evaluating and producing shale gas: Society of Petroleum Engineers Unconventional Gas Conference, Pittsburgh, Pennsylvania, February 23–25, 2010, SPE Paper 131768, 34 p., doi:10.2118/131768-MS.

Sondergeld, C. H., R. J. Ambrose, C. S. Rai, and J. Moncrieff, 2010b, Microstructural studies of gas shales: Society of Petroleum Engineers Unconventional Gas Conference, Pittsburgh, Pennsylvania, February 23–25, 2010, SPE Paper 131771, 17 p., doi:10.2118/131771-MS.

Stach, E., et al., 1982, Stach's textbook of coal petrology, 3d ed.: Berlin, Germany, Gebrüder Borntraeger, 535 p.

Tannenbaum, E., and Z. Aizenshtat, 1984, Formation of immature asphalt from organic-rich carbonate rocks. Part II: Correlation of maturation indicators: Organic Geochemistry, v. 6, p. 503–511, doi:10.1016/0146-6380(84)90073-1.

Tannenbaum, E., and Z. Aizenshtat, 1985, Formation of immature asphalt from organic-rich carbonate rocks. Part I: Geochemical correlation: Organic Geochemistry, v. 8, p. 181–192, doi:10.1016/0146-6380(85)90037-3.

Tannenbaum, E., B. J. Huizinga, and I. R. Kaplan, 1986, Role of minerals in thermal alteration of organic matter. Part II: A material balance: AAPG Bulletin, v. 70, p. 1156–1165.

Taylor, G. H., S. Y. Liu, and M. Teichmuller, 1991, Bituminite: A TEM view: International Journal of Coal Geology, v. 18, p. 71–85, doi:10.1016/0166-5162(91)90044-J.

Taylor, G. H., M. Teichmüller, A. Davis, C. F. K. Diessel, R. Littke, and P. Robert, 1998, Organic petrology: Berlin, Germany, Gebrüder Borntraeger, 704 p.

Teerman, S. C., B. J. Cardott, R. W. Harding, M. J. Lemos De Sousa, D. R. Logan, H. J. Pinheiro, M. Reinhardt, C. L. Thompson-Rizer, and R. A. Woods, 1995, Source rock/dispersed organic matter characterization: TSOP research subcommittee results: Organic Geochemistry, v. 22, p. 11–25, doi:10.1016/0146-6380(95)90004-7.

Thompson-Rizer, C. L., 1987, Some optical characteristics of solid bitumen in visual kerogen preparations: Organic Geochemistry, v. 11, p. 385–392, doi:10.1016/0146-6380(87)90071-4.

Tissot, B. P., and D. H. Welte, 1984, Petroleum formation and occurrence: Berlin, Germany, Springer Verlag, 699 p.

Zagorski, W. A., D. A. Bowman, M. Emery, and G. R. Wrightstone, 2010, An overview of some key factors controlling well productivity in core areas of the Appalachian Basin Marcellus Shale play, *in* D. M. Jarvie et al., eds., Critical assessment of shale resource plays (abs.): AAPG/Society of Exploration Geophysicists/Society of Petroleum Engineers/Society of Petrophysicists and Well Log Analysts Hedberg Research Conference, Austin, Texas, December 5–10, 2010, 1 p.